

Evaluating the Euler-Euler approach for predicting a strongly 3D bubble induced recirculatory flow with OpenFOAM

Duguay, Jason^{a,*}, Lacey, Jay^a, Massé, Alexandre^b

^aUniversité de Sherbrooke, 2500 boul. de l'Université, Sherbrooke, QC.

^bLaSalle|NHC Ltd. 9620 Saint-Patrick Street, LaSalle, QC.

FOR COMMENT

Abstract

Municipal wastewater treatment plants use bubbly flows to assist in settling out sediment from the plant's influent. Computational fluid dynamics (CFD) is an attractive tool to virtually prototype grit-chamber designs to improve sediment deposition in their complex 3D flow field. This study assesses the ability of a two-phase unsteady Reynolds-averaged Euler-Euler approach (uRANS-EE) to predict bubble induced recirculatory flow in a laboratory tank of similar complexity to that expected in a full-scale grit-chamber. The sensitivity of the model to various combinations of interphase momentum transfer terms is discussed. Numerical results are validated against an experimental data set consisting of stereoscopic particle image velocimetry (sPIV), void fraction profiles and bubble rise-velocities (\bar{w}_a). Numerical predictions of the volumetric fluid flux returning towards the diffuser ($\bar{\Phi}_{neg}$) through a lateral cross-section of the flow varied between 60 to 97% of the experimental flux, depending on the combination of interphase momentum transfer terms used. High in the bubble swarm, predicted \bar{w}_a exceeded measured values by a factor of 1.15 to 1.75. Lower in the swarm, numerical \bar{w}_a more closely approximated experimental values. Near bed velocities were underpredicted by upwards of 25% and the models had difficulty replicating the flow field near the far wall of the tank. A study on the effects of the lateral lift term demonstrated improved estimates of volumetric flux and near-bed velocities with lift coefficients as high as 1.25. This study examines the strengths and weaknesses of the uRANS-EE method for predicting a complex 3D multiphase flow and will be of interest to practitioners in wastewater treatment and other fields applying bubbly air-water flows.

Keywords: Multiphase flow, OpenFOAM, twoPhaseEulerFoam, Euler-Euler, stereoscopic particle image velocimetry, computational fluid dynamics, grit chamber, wastewater treatment

1. Introduction

Two-phase flows appear in numerous fields of engineering. They are essential to many industrial mixing processes, chemical reactions and civil engineering applications. Bubbly flows are a common two-phase flow, in which the movement of a dispersed rising gas (e.g., air bubbles), is coupled to the movement of a surrounding continuous liquid phase (e.g., water). Bubbly flows are used at waste-water treatment plants to induce an axially recirculating flow pattern in grit removal chambers. This permits heavier solids, termed grit (i.e., small gravel, sand), to settle early in the treatment process while maintaining lighter organic solids in suspension for later biological treatment (Brenner and Diskin, 1992). A standard grit-chamber functions as follows; air is injected low in the water column near one wall of the grit chamber, momentum transfer between the rising bubble swarm and surrounding water causes the water to accelerate upwards, which in turn entrains adjacent water into the bubble swarm. At steady state, a recirculatory flow is established.

Sediment settling efficiency is important for grit-chamber design. Grit remaining in suspension after exiting

the chamber will eventually settle farther downstream in the treatment process, requiring operational downtime and resources to remove. Grit removal efficiency can be improved by; modifying the grit-chamber's geometry, adjusting the axial rate of rotation of the recirculatory flow (i.e., by varying injected air flow rates) or optimally managing sediment and waste-water fluxes. Optimizing grit-chamber operation using physical models is difficult due to the challenge of simultaneously scaling fluid, bubble and sediment properties alongside the physical geometry of the chamber. In situ study of grit-chambers is difficult because of their large spatial scales ($> 16 \text{ m}^2$ in section and 100 m long), limited access for instrumentation, and imprecise or missing operational data (e.g., injected air flow rates, bubble size distributions, sediment and fluid fluxes). Considering these challenges, computational fluid dynamics (CFD) presents a promising alternative to the experimental study of grit-chamber efficiency.

Two-phase CFD approaches for modeling bubbly flows have developed considerably in the past two decades. Since appearing in its high void fraction form (Rusche, 2002), the two-phase Euler-Euler method has been applied to the study of bubble column reactors (Marschall et al., 2011a,b; Khan et al., 2017; Bhusare et al., 2017, 2018), stirred tanks (Kerdouss et al., 2006; Shi and Rzebak, 2018), gas-mixed anaerobic digesters (Wei et al., 2019), fluidized reactor

*Corresponding author

Email address: jason.duguay@usherbrooke.ca (Duguay, Jason)

beds (Liu and Hinrichsen, 2013; Gosavi et al., 2018) and multi-phase gravitational separation tanks (Panda et al., 2017). Direct two-phase CFD modeling of grit chambers has received little attention (e.g., Dutta et al. (2014) who modeled sediment in water without bubbles), and the flows studied in the previous works are unlike the 3D helical recirculatory flow expected in an aerated grit chamber. However, a few recent studies have made gains in this area. Notably, Balleda et al. (2007) and Ali Basheer and Subramaniam (2012) investigated the Euler-Euler approach to model the bubble induced recirculatory flow in a baffled chamber. Dapelo et al. (2015) employed a hybrid Euler-Lagrangian volume-of-fluid (VOF) method to simulate bubble induced mixing in an axisymmetric bioreactor. These authors (Balleda et al., 2007; Ali Basheer and Subramaniam, 2012; Dapelo et al., 2015) found the modeling approaches applied to have predicted measured flow field metrics obtained using 2-dimensional 2-component particle image velocimetry (2D-2C PIV) comparatively well. However, the flow in these studies, though recirculatory, were only quasi-3D in character and presented less complexity than expected in an aerated grit chamber. Prior to investigating multiphase Eulerian methods to model sediment transport within a full-scale aerated grit chamber (sediment, water and air), it is first desirable to evaluate the unsteady Reynolds averaged two-phase Euler-Euler (water and air) approach's ability to model a complex bubble induced 3D turbulent flow field.

Herein we apply OpenFOAM's *twoPhaseEulerFoam* solver to model bubble induced recirculation in a laboratory water tank operating over a range of air mass flow rates. Preliminary visualization of this simple geometry's flow field revealed a complex, air flow rate sensitive 3D flow structure approximating the level of complexity expected in a grit-chamber, without the need to induce a helical cross-flow. A combination of experimental methods are used to provide a robust data set for the validation of the CFD results. To evaluate the model's ability to reproduce the 3D flow structure in the experiment, a central portion of the tank's time-averaged volumetric 3-dimensional 3-component (3D-3C) velocity field is reconstructed using a multi-plane stereoscopic particle image velocimetry technique (sPIV). The time-averaged recirculating volumetric flux ($\bar{\Phi}_{neg}$), an important bulk flow metric, passing through a lateral cross-section of the tank is estimated from the 3D-3C flow field data. Stereoscopic PIV is also applied to characterize the 2D-3C component flow field across the central longitudinal plane of the tank. Void fraction profiles (i.e., temporal density of bubbles) are measured across the rising bubble swarm using an optical probe. Rise velocity and bubble diameter distributions were acquired from high-speed videography (HSV) taken of the bubble swarm. The sensitivity of modelled results to a variety of interfacial momentum transfer term combinations (i.e., drag, lateral lift, virtual mass, turbulent dispersion), with and without swarm corrections, and a range of mean bubble diameters is assessed. The effects of these combinations on predicting the measured 3D-3C flow field, recirculatory volumetric flux, centerline turbu-

lent velocity field, bubble swarm morphology, and bubble rise velocities are also discussed. This study presents a comprehensive evaluation of the model's ability to predict important two-phase flow fields and should be of interest to those intending to apply such an approach to model similar bubble driven recirculatory flows.

2. Methods and Materials

2.1. Numerical method

This study aims to validate OpenFOAM's 5.0 *twoPhaseEulerFoam* solver for modeling bubble induced recirculatory flow. In the solver's documentation (Green-shields, 2017), *twoPhaseEulerFoam* is stated to solve "... a system of 2 compressible fluid phases with one phase dispersed, e.g. gas bubbles in a liquid including heat-transfer". The general approach of the two-fluid Euler-Euler method is presented in this section. Addition details on its implementation and solution procedures are available in Rusche (2002); Behzadi et al. (2004); Bhusare et al. (2017).

In the Euler-Euler method both phases are modeled as interpenetrating continua, permitting the transfer of momentum between them. For each phase (φ), a Reynolds averaged continuity (Eq. 1) and momentum equation (Eq. 2) are solved. The averaging process introduces terms requiring expressions in terms of mean variables to provide closure. In Eqs. 1 and 2, overbars indicate Reynolds averaged mean components, α_φ and $\bar{\mathbf{U}}_\varphi$ are the phase fraction and velocity, $\bar{\rho}_\varphi$ denotes density, temporal terms contain ∂_t , $\bar{\mathbf{R}}_\varphi^{eff}$ is the effective Reynolds stress tensor (combined viscous and Reynolds turbulent stresses), \bar{p} and \mathbf{g} denote pressure and gravitational acceleration respectively. $\bar{\mathbf{F}}_\varphi$ is the sum of the inter-phase forces responsible for momentum transfer between the dispersed and continuous phases. Both Reynolds stresses and momentum transfer terms appear as a result of the averaging process. The approaches used to account for their effect on the flow field are described in the following subsections.

$$\frac{\partial \alpha_\varphi}{\partial t} + \nabla \cdot (\alpha_\varphi \bar{\mathbf{U}}_\varphi) = 0 \quad (1)$$

$$\begin{aligned} \frac{\partial \alpha_\varphi \bar{\mathbf{U}}_\varphi}{\partial t} + \nabla \cdot (\alpha_\varphi \bar{\mathbf{U}}_\varphi \bar{\mathbf{U}}_\varphi) + \nabla \cdot (\alpha_\varphi \bar{\mathbf{R}}_\varphi^{eff}) = \\ -\alpha_\varphi \nabla \bar{p} + \alpha_\varphi \mathbf{g} + \frac{\sum \bar{\mathbf{F}}_\varphi}{\rho_\varphi} \end{aligned} \quad (2)$$

2.1.1. Interphase momentum transfer

The recirculatory motion induced in the body of water adjacent to a rising bubble swarm is a function primarily of the interfacial momentum transfer term $\bar{\mathbf{F}}_\varphi$ in Eq. 2. This term can be deconstructed into four principal momentum transfer processes. These include (1) the drag force ($\bar{\mathbf{F}}_D$) acting on the rising bubbles, (2) the lateral lift force ($\bar{\mathbf{F}}_L$) due to unbalanced pressure distributions over the bubble's surface in a shear flow, (3) the virtual mass force ($\bar{\mathbf{F}}_{VM}$)

necessary to accelerate a small quantity of the fluid adjacent to a bubble as it rises and (4) the turbulent dispersion force ($\bar{\mathbf{F}}_{TD}$) caused by turbulent fluctuations in the continuous phase. The following subsections present the necessary background for each of these momentum transfer processes and the closure methods investigated herein to simulate their effects.

Drag force

An air bubble rising with a velocity $\bar{\mathbf{U}}_a$ in water with a local velocity $\bar{\mathbf{U}}_w$ will have a relative (slip) velocity $\bar{\mathbf{U}}_r$ within the reference frame of the apparatus. The rising bubble will experience a retarding drag force ($\bar{\mathbf{F}}_D$, Eq. 3) in the direction opposite to the bubble's trajectory. The magnitude of this force depends on the bubble's shape and associated drag coefficient (C_D), the density of the continuous phase (ρ_w), where the subscript w indicates the continuous phase (i.e., water) and the diameter of the bubble (d_a), where the subscript a represents the dispersed (i.e., air) phase. The drag coefficient is a function of the bubble's Reynolds number (Eq. 4) which depends on the slip velocity, the kinematic viscosity (ν_w) of the continuous phase and d_a . A number of approaches are available to determine C_D for dispersed bubble flows. We tested two prominent formulations for C_D which are presented in the following paragraphs.

$$\bar{\mathbf{F}}_D = \frac{3}{4} \alpha_a C_D \frac{\bar{\rho}_w}{d_a} |\bar{\mathbf{U}}_r| \bar{\mathbf{U}}_r \quad (3)$$

$$Re \equiv \frac{d_a |\bar{\mathbf{U}}_r|}{\nu_w} \quad (4)$$

The Schiller-Naumann (*SN*) model (Eq. 5) has been widely applied for modeling drag on small spherical uniform bubbles. At lower Reynolds numbers (i.e., $Re \leq 1000$) a power law (Eq. 5) is used to predict C_D . For bubbles at higher Re (i.e., $Re \geq 1000$), C_D is taken to be a constant 0.44.

$$C_D = \begin{cases} \frac{24}{Re} (1 + 0.15 Re^{0.687}) & \text{if } Re \leq 1000 \\ 0.44 & \text{if } Re \geq 1000 \end{cases} \quad (5)$$

The Ishii-Zuber (*IZ*) correlation for C_D was developed for modeling densely dispersed bubbly flows (Ishii and Zuber, 1979). The presumption of the model is that at high bubble concentrations, the effective mixture viscosity increases, causing an increase in the drag force. The mixture viscosity (μ_m , Eq. 6) is a function of α_a , the dynamic viscosity of the continuous phase (μ_w) and the exponent A (Eq. 7, where μ_a is the dynamic viscosity of the air phase):

$$\mu_m = \mu_w (1 - \alpha_a)^A \quad (6)$$

$$A = -2.5 \left(\frac{0.4\mu_w + \mu_a}{\mu_w + \mu_a} \right). \quad (7)$$

The mixture Reynolds number is then obtained with Eq. 8:

$$R_{em} = \frac{\rho_w d_a |\bar{\mathbf{U}}_r|}{\mu_m}. \quad (8)$$

The choice of C_D depends on whether the bubbles are in the spherical or ellipsoidal regime. To determine the regime, the C_D^s (where s indicates spherical) is first calculated using Eq. 5, with R_e replacing R_{em} . Then determining C_D^e (where e indicates ellipsoidal) using Eqs. 9 to 11, where E_o is the Eötvös number (Eq. 10, σ is the surface tension coefficient, $\Delta\rho$ difference in phase density):

$$C_D^e = \frac{2}{3} \sqrt{E_o} \left[\frac{1 + 17.67f(\alpha_a)^{6/7}}{18.67f(\alpha_a)} \right] \quad (9)$$

$$f(\alpha_a) = \frac{\mu_w}{\mu_m} \sqrt{1 - \alpha_a} \quad (10)$$

$$E_o = \frac{\Delta\rho g d_a^2}{\sigma}. \quad (11)$$

Finally, if the bubbles are sufficiently ellipsoidal (i.e., $C_D^e > C_D^s$), then;

$$C_D = \min \left[C_D^e, Re \frac{8}{3} (1 - \alpha_a) \right]. \quad (12)$$

Else if the bubbles are spherical (i.e., $C_D^e < C_D^s$), then;

$$C_D = C_D^s. \quad (13)$$

Swarm effects

A swarm correction term is used in applications where C_D correlations designed for a single isolated bubble fail when bubbles rise in dense swarms. The swarm effect generally increases the value of C_D beyond that calculated using a drag coefficient model. A swarm correction aims to simulate this increase in C_D (i.e., $C_{D,s}$). A widely applied swarm correction proposed by (Tomiyama et al., 1995) is presented in Equation 14. The exponential coefficient l is recommended to be 1.75 (Tomiyama et al., 1995).

$$C_{D,s} = C_D \alpha_a^{3-2l} \quad (14)$$

Lateral lift force

Bubbles tend to laterally migrate due to unbalanced forces on the bubble's surface caused by local vorticity in the continuous phase ($\bar{\omega}_w$) (Zhongchun et al., 2014). The lateral lift force ($\bar{\mathbf{F}}_L$, Eq. 15) is caused by wake eccentricities locally varying pressures applied on the surfaces of the bubble as it rises through a shear flow (Tomiyama et al., 2002). Generally, a positive lateral lift force coefficient (C_l) is used for small spherical bubbles of low Eötvös number, as is the case in this study. However, there is no consensus on a universally appropriate constant value for C_l , and various researches have reported good predictions of experimental results using values of C_l between 0.01 to 0.5 (Yeoh and Tu, 2006; Lubchenko et al., 2018; Colombo and Fairweather, 2019). A common value of C_l is 0.5 (Marschall et al., 2011a), which was found to be the theoretical value for a clean bubble in inviscid flow Behzadi et al. (2004); Auton (1987). Here the C_l was taken as 0.5,

however, a sensitivity analysis is presented later (see 3.8) examining how higher values of C_l modify features of the bubble swarm and the recirculatory flow.

$$\bar{\mathbf{F}}_L = \alpha_a \bar{\rho}_w C_L \cdot (\bar{\mathbf{U}}_r) \times \bar{\boldsymbol{\omega}}_w \quad (15)$$

$$\bar{\boldsymbol{\omega}} = \nabla \times \bar{\mathbf{U}}_w \quad (16)$$

Virtual mass force

A rising bubble will transfer momentum to the continuous phase as it accelerates small quantities of fluid immediately in its path during ascent. This process results in the interfacial virtual mass force ($\bar{\mathbf{F}}_{VM}$, Eq. 17, where D_i indicates the substantial derivative). For spherical bubbles, the virtual mass coefficient C_{VM} is found to be 0.5 (Marschall et al., 2011a). For non-spherical bubbles C_{VM} is usually smaller. In this study, C_{VM} was taken to be equal to 0.5.

$$\bar{\mathbf{F}}_{VM} = C_{VM} \alpha_b \bar{\rho}_w \left(\frac{D_a \bar{\mathbf{U}}_a}{D_t} - \frac{D_w \bar{\mathbf{U}}_w}{D_t} \right) \quad (17)$$

$$\text{where, } \frac{D_i}{D_t} = \frac{\partial}{\partial t} + \nabla \bar{\mathbf{U}}_i \quad (18)$$

Turbulent dispersion forces

Turbulence induced mixing of bubbles from regions of high air concentrations (air phase fraction) to regions of low concentrations of air are caused by turbulent dispersion forces ($\bar{\mathbf{F}}_{TD}$). Equation 19 shows that $\bar{\mathbf{F}}_{TD}$ is a function of the turbulent dispersion coefficient C_{TD} , the mean kinetic energy k and the gradient of the discrete phase fraction. Generally, C_{TD} is set to a value between 0.1 and 1, with most studies opting for a value of 0.5 (Marschall et al., 2011a).

$$\bar{\mathbf{F}}_{TD} = C_{TD} \bar{\rho}_w k \nabla \alpha_a \quad (19)$$

2.1.2. Turbulence modeling

The mixture $k - \epsilon$ model (distributed with the standard release of OpenFOAM 5.0) was applied to determine the turbulent viscosity necessary for closure of the $\bar{\mathbf{R}}_{eff}$ term in Eq. 2. The details of the model's implementation are available in Behzadi et al. (2004) and for brevity are not presented here. The presumption of the mixture $k - \epsilon$ model is that as air fraction increases, turbulence in the continuous phase becomes less important as the continuous phase occupies a smaller volume of interstitial space between bubbles. At high air fractions, the dispersed phase (i.e., air bubbles) can become continuous (phase-inversion) and its turbulence dominates. The mixture $k - \epsilon$ turbulence closure model accounts for the relative turbulence contributions from each phase and provides a more robust approach to modeling turbulence in both low and high phase fraction flows compared to approaches only considering turbulence in the continuous phase (Behzadi et al., 2004). The model proposed by Behzadi et al. (2004) is slightly modified in OpenFOAM 5.0 to include an effective

density for the gaseous phase and an alternative bubble-generated turbulence model outlined in Lahey (2005).

2.2. Experimental apparatus

Experimental data used to validate numerical results were obtained in a 400 mm long x 205 mm wide x 250 mm high glass walled transparent tank (Fig. 1). To establish a bubble induced recirculatory flow in the tank, air was injected through a porous aeration stone fixed laterally to the bottom of the tank using an air pump with a maximum capacity of 15 l/min. The stone was centered along the central lateral axis ($y = 0$ mm) of the tank and positioned so its back face was 5 mm from the back wall of the tank (i.e., 5 mm along the longitudinal axis of the tank x). The sides and bottom of the stone were epoxied to block its porosity. A laterally centralized region of the upper face of the stone (70 mm x 35 mm, area = 2.625x10³ mm²) was left porous for air to exit (i.e., the *inlet*).

Three mass flow rates (\dot{m}_a) of air were supplied to the stone to provide a range of validation data of the turbulent velocity field for comparison with *twoPhaseEulerFoam*. Details of the three flow rates tested, their equivalent volumetric flow rates (Q_{air} , l/min) and resulting average superficial velocities expected over the inlet surface (v_a , m/s) are presented in Table 1. In all experiments, the water level in the tank was set to 205 mm. Water temperature and ambient air temperature during data acquisition was 22 °C.

2.3. Air flow measurement

Volumetric air flow rates were measured with a rotometer (Aalborg, Orangeburg, New York, part P11A1-BB0A-034-39-ST, ± 2% full scale). Temperature (T) in the supply line was measured with a precision Thomas Scientific digital thermometer (part 9329H03, ± 0.2 °C). Gauge pressures in the supply line downstream of the rotometer were recorded using a digital manometer (Dwyer 475-4-FM, 10 psi (68.9 kPa), ± 0.5% full scale). Ambient absolute pressure in the laboratory was measured with LPS25H barometric pressure sensor (ST, Shanghai, China, 80-110 kPa, ± 0.02 kPa absolute accuracy pressure over temperature). The ideal gas law (Eq. 20; R gas constant for dry air, 8.314 J/molK; M molar mass of dry air, 28.9647e⁻³ kg/mol) was used to calculate the density of air ρ_a . The mass flow rate (\dot{m}_a) was then calculated as the product of the measured volumetric air flow rate and ρ_a . Temperatures within the supply line were 23.5 ± 1 °C. During preliminary trials, the minor variations in ambient temperature and pressure observed over the period of two weeks were found to have a negligible effect on ρ_a . Therefore, volumetric air flow rates during all experiments were set by adjusting the precision rotometer valve to place the center of the ball to the following scale readings; low flow - 29 mm, medium flow - 57 mm and, low flow - 85 mm. The stability of ambient pressure and temperature during experiments were nevertheless monitored. The three volumetric flow rates, corresponding mass flow rates and superficial velocities over the inlet are presented in Table 1.

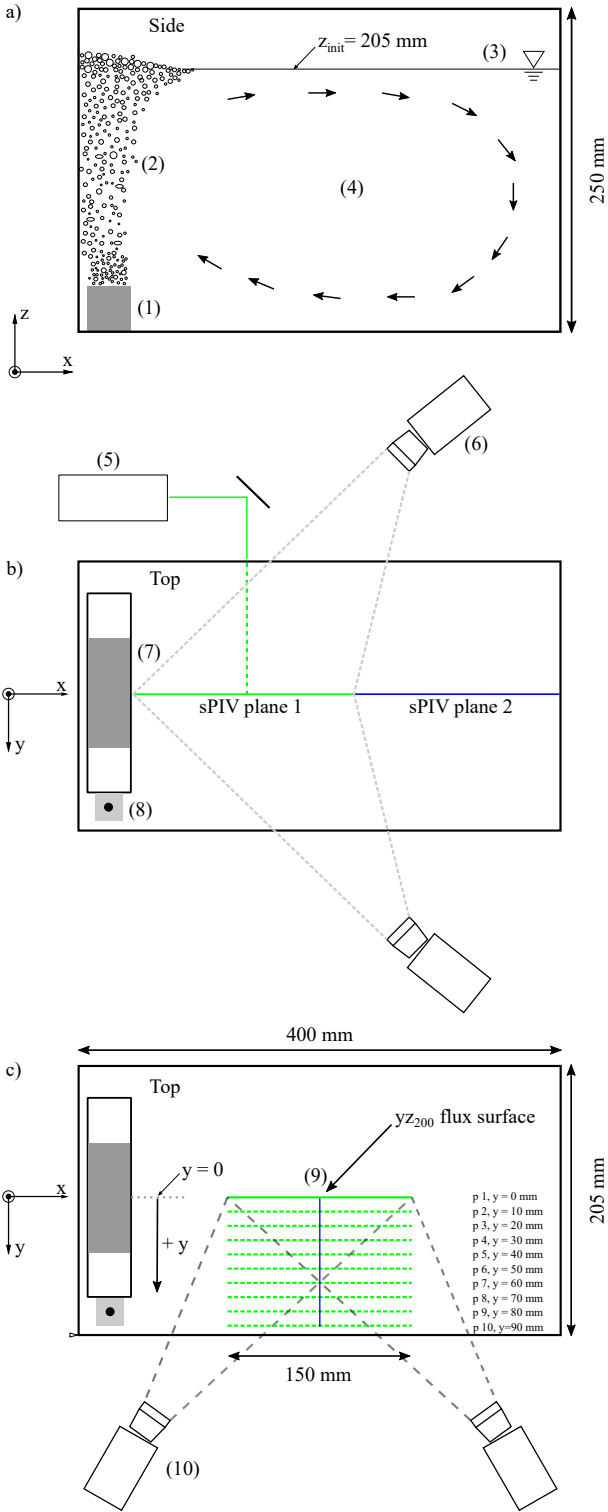


Figure 1: Experimental apparatus used to acquire validation data for numerical trials. Side view of tank (a) with air stone (1), bubble swarm (2), free surface (3) and general pattern of recirculatory flow (4). Top view of lateral centerline sPIV experimental setup (b) laser light source (5), stereo HSV camera configuration (6), air bubble diffuser surface (7), air inlet to stone (8). Top view (c) of plane positions (9) and camera arrangement (10) used to acquire time-averaged 3-D flow field of volume. Blue line indicates position of laterally orientated yz_{x200} plane used to integrate Φ_{neg} .

$$\rho_a = \frac{pM}{RT} \quad (20)$$

Table 1: Experimental parameters

Exp.	Q_a (l/min)	\dot{m}_a (g/min)	v_a (m/s)
1	3.3	4	0.0227
2	6.6	8	0.0446
3	9.7	12	0.0657

2.4. Void fraction

Spatial void fraction distributions were measured using a phase detection optical probe (A2 Photonic Sensors, Grenoble, France). Optical probes record the residence time of bubbles passing over the fiber optic probe tip and express this time as a fraction of the total sampling time to obtain time-averaged void fraction measurements. The instrument detects bubbles at high temporal resolution (500 Hz) by measuring the differences in the refractive indices of water and air (Enrique Juliá et al., 2005).

Void fractions were measured over four horizontal profiles above the center-line of the stone ($x = 22.5$ mm) for each value of \dot{m}_a . The first profile of 8 points was located 10 mm above the stone (z'), the remaining profiles each had 11 points and were positioned at $z' = 50$ mm, $z' = 100$ mm and $z' = 150$ mm. Points were laterally spaced along the positive y direction by 5 mm, with the first point in a row beginning at the lateral center-line of the tank at $y = 0$. The time-averaged void fractions of the bubble plume were verified to be symmetrical across the lateral center-line axis of the tank by taking additional comparative measurements at mirrored locations on the other side of the lateral centerline (not presented herein). In the numerical models the time-averaged scalar quantity $\bar{\alpha}_a$ (*alpha.air*), representing the air void fraction in the numerical model, was extracted from the numerical results at the same locations sampled experimentally.

2.5. Bubble diameter and rise velocity distributions

A Phantom Miro M110 high-speed video camera fitted with a 1:1 macro lens (Nikon AF-D Micro-Nikkor 60mm f2.8D) was used to record video of the rising bubble swarm. Recordings were taken at two vertical positions above the top of the diffuser stone; $z' = 50$ mm and $z' = 150$ mm. The field of view (FOV) was 30 mm high and 45 mm wide and was centered laterally along the width of the tank (at $y = 0$). The focus plane of the camera was positioned at $x = 10$ mm from the wall. A calibration plate was used to align the focus plane and determine a linear scaling ratio of 26 px/mm. The depth of focus was sufficiently thin that only bubbles near ($\approx \pm 1.5$ mm) the face of the calibration plate were sharply in focus. Positioning the focus plane at $x = 10$ mm allowed in-focus bubbles to not be occluded by out-of-focus bubbles between the glass tank wall and the focus plane.

For each value of \dot{m}_a , the long and short axis of 100 randomly selected bubbles were measured from 20 second recordings obtained at 400 Hz. Bubble rise velocities were calculated using Equation 21, where h_{FOV} is the height of the field of view ($h_{FOV} = 46$ mm), N_{FOV} is the number of frames required for the bubble to pass through h_{FOV} , and dt is the time-step between each frame (i.e., 0.0025 s). The widths, heights and N_{FOV} of bubbles with $> 50\%$ of their surface in focus were measured.

$$v_r = \frac{h_{FOV}}{N_{FOV} dt} \quad (21)$$

2.6. Free surface bulking measurements

Backlit calibrated high-speed video of the free surface was taken with the center of the camera's field of view positioned at $y = 0$ and $z = 205$ mm (the resting water surface level) looking through the glass of the tank nearest the diffuser (i.e., $x = 0$ mm). The camera's plane of focus was positioned at $x = 10$ mm, with an approximate ± 1.5 mm depth of field. Videos of the free surface bulking were taken over a 60 s period for each \dot{m}_a condition. Backlighting produced a sharp grayscale gradient between the bubbly water (dark, 115 counts) and the atmosphere (white, 255 counts). A weighted accumulator function (Python 3.6 OpenCV cv2.accumulateWeighted) was applied to the video frames to obtain time averaged images of the free surface. The range of free-surface bulking was defined as that over which the time-averaged pixel intensities varied from dark (115 counts) to nearly white (255 counts). The time averaged vertical position of the free surface was taken as the center of this range (185 counts). Free surface bulking estimates in the numerical results were obtained in ParaView by taking a lateral slice of the time-averaged domain at $y = 0$, applying a time-averaged alpha.air threshold of 0.5 and measuring the z position of the threshold's contour in the cell adjacent to the $x = 0$ mm wall.

2.7. Flow field measurement

Two sets of particle image velocimetry experiments were performed to measure the flow field. The first experiment used planar stereoscopic particle image velocimetry (sPIV) to measure over the lateral centerline ($y = 0$), x - z plane for each \dot{m}_a condition. The second experiment used sPIV over 10 laterally positioned planes to reconstruct the central time-averaged 3D flow field of the tank at \dot{m}_a 12 g/min. The details of both experiments are outlined below.

In PIV experiment 1, two sPIV planes (*near* and *far* from the stone) were combined to provide a complete measurement of the flow field over the central lateral axis ($y = 0$) of the tank (Fig. 1b). The *near* position spanned from $40 \text{ mm} < x < 200 \text{ mm}$ and the *far* from $200 \text{ mm} < x < 400 \text{ mm}$. The flow was illuminated with a Litron LDY303 Nd:YLF dual cavity Q-switched laser with a maximum output energy of 20 mJ. Seeding concentrations were optimized to obtain a minimum of 4 particles per 16×16 px interrogation window. The laser light sheet was diverged using a -15 mm concave lens and thinned by a 500 mm convex convergent lens. Cameras were fitted with 50

mm Nikkon lens (AF NIKKOR 50mm f/1.4D). Eighty seconds of single frame sPIV measurements at 200 Hz were measured for each \dot{m}_a . Image acquisition and vector processing were performed in DaVis version 8.3.1. Decreasing 3 pass (i.e., 64×64 px, 32×32 px, 16×16 px) stereo cross-correlation was performed. A median 2 standard deviation vector removal and replacement filter was applied on the intermittent and final vector fields. The spatial resolution of the vector field was 16 pixels with a 50% interrogation window overlap, providing a vector field with a spatial resolution of approximately 1.2 mm. The flow field close to the water surface, $z > 180$ mm, was not considered due to spurious vectors caused by light reflections off surface bubbles. Reflections also rendered flow field measurements impossible near and within the bubble swarm ($x < 40$ mm).

In PIV experiment 2, ten sPIV measurements planes were taken in the $\dot{m}_a = 12$ g/min condition using the method outlined for PIV experiment 1. Planes were spaced at $\Delta_y = 10$ mm starting from $y = 0$ mm and ending at $y = 90$ mm (Fig. 1c). The planes spanned longitudinally between $120 \text{ mm} < x < 280 \text{ mm}$ and vertically between $0 \text{ mm} < z < 175 \text{ mm}$. Flow field values obtained over the 10 planes were interpolated to a 3D, 5 mm cube grid with total dimensions of (160 mm x 90 mm x 160 mm). The resulting volume is used to evaluate flux over a lateral cross-sectional plane of the flow field and to provide insights on its 3-D structure.

In both PIV experiments, time averaged velocity components (i.e., \bar{u} , \bar{v} , \bar{w}) were derived by taking the temporal average of instantaneous velocity measurements. Turbulent intensities were calculated as the standard deviation of the instantaneous velocity measurements (i.e., \bar{u}' , \bar{v}' , \bar{w}'). Turbulent kinetic energy (k) was calculated as $k = 0.5(\bar{u}'^2 + \bar{v}'^2 + \bar{w}'^2)$.

2.8. Volumetric fluid flux through yz_{x200} -plane

The accuracy of the numerical approaches at predicting the recirculatory flow of the tank was partially assessed by comparing the time-averaged flux returning towards the diffuser through a lateral slice (yz -plane) of the tank with that estimated experimentally from sPIV data. The fluid flux directed in the negative x direction ($\bar{\Phi}_{neg}$) (i.e., towards the diffuser Fig. 1) over a yz -plane positioned at $x = 200$ mm (yz_{x200} -plane) was calculated from temporally averaged and spatially interpolated from sPIV data obtained in experiment 2. Because of the axisymmetric nature of the flow field, $\bar{\Phi}_{neg}$ values presented herein are for only one half of the lateral span of the tank. Practical limitations of the sPIV experiment restricted sampling to below $z = 180$ mm and $y > 12.5$ mm. However, the method permitted $\bar{\Phi}_{neg}$ to be measured over the majority of the plane. $\bar{\Phi}_{neg}$ was calculated using Eq. 22, which is conditional that $\bar{u}_w < 0$ (i.e., returning towards the diffuser).

$$\bar{\Phi}_{neg} = \iint_S \bar{\mathbf{U}}_w \cdot \hat{n} dS \mid \bar{u}_w < 0 \quad (22)$$

2.9. Spatial and temporal convergence

Preliminary simulations demonstrated the numerical results were sensitive to the wall-normal cell size on the wall nearest the bubble swarm. This is attributable to the strong velocity gradients in both phases in this region and sensitivities of the wall functions applied on this boundary. A sensitivity analysis was performed to identify an appropriate wall-normal cell size. With all other variables held constant, the following four wall-normal cell sizes adjacent to the bubble swarm were tested: 1 mm, 1.25 mm, 1.667 mm and 2.5 mm. Time averaged $\bar{\Phi}_{neg}$ for each simulation were 0.703 l/s, 0.725 l/s, 0.697 l/s, 0.668 l/s, respectively (measured $\bar{\Phi}_{neg} = 0.77$ l/s, see section 3.2). The 1.25 mm cell size provided the closest prediction of the bulk variable $\bar{\Phi}_{neg}$. Based on these findings, a layer of 5, 1.25 mm cells was used to refine the flow near the wall adjacent to the rising bubble swarm.

Sensitivity of the results to the cell size throughout the rest of the domain was also assessed. Details of the parameters studied and results of this analysis are presented in Table 2. From Table 2, convergence of the bulk variable $\bar{\Phi}_{neg}$ is observed with decreasing cell size. Mesh 2 (1.85 mm) closely approximates (0.746 l/s) the experimentally estimated $\bar{\Phi}_{neg}$ of 0.77 l/s (see section 3.2). Exceptionally, the finest grid (mesh 1) was found to under-predict $\bar{\Phi}_{neg}$ (0.690 l/s). A vertical plot of \bar{u} in the water phase taken at $x = 0.2$ m, $y = 0.1025$ m for each of the five meshes is presented in Fig. 2. It is evident from Fig. 2 that meshes 4, 5 and 6 are not converged. The remaining finer meshes closely approximate each other. Mesh 2 was retained to discretize the domains of the final simulations given the observed spatial convergence, the accuracy of the $\bar{\Phi}_{neg}$ prediction and taking computation time into consideration (33.33 hours on mesh 2, compared to 80.24 on mesh 1).

Because *twoPhaseEulerFoam* is a transient solver, temporal convergence of the simulation over the averaging period was also assessed. Velocity components at each timestep were monitored at three locations above the longitudinal and lateral center of the bottom of the tank ($x = 0.2$ m, $y = 0.1025$ m) at $z = 0.05$ m, $z = 0.10$ m and $z = 0.15$ m. The relative standard deviations (σ_u/\bar{u}) of u at these points expressed as percentages were respectively: 2.50%, 2.29% and 3.7%. These values indicate a level of variability over the averaging period sufficiently low to conclude temporal convergence.

2.10. Mesh

Because the geometry to be modeled only contained right-angles, a hexahedra mesh was used to discretize the domain. The 3D mesh was constructed using OpenFOAM's native *blockMesh* utility using 39 blocks. The in-house interactive Python graphical user interface (GUI) *blockMeshBuilder* package (written with VTK's Python bindings) was used to efficiently (in only 10 lines of code) construct the complicated multi-block mesh. The GUI allows the user to interactively select patch faces to add to boundary condition groups (Link to download). Axial symmetry was assumed across the central lateral axis to

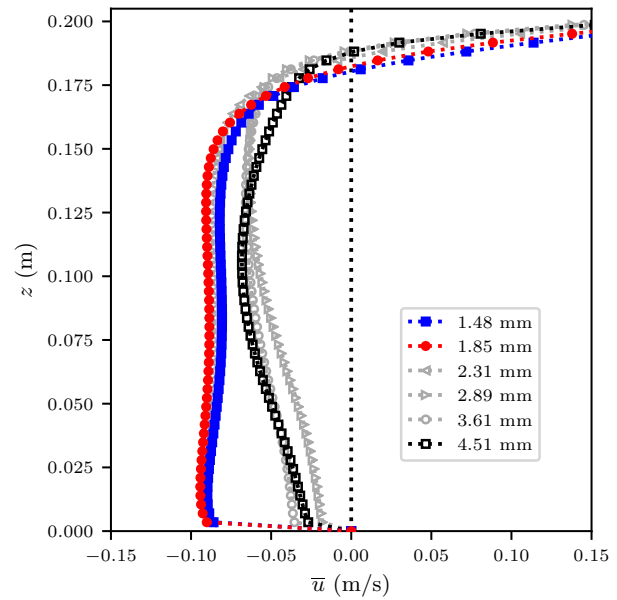


Figure 2: Vertical profiles of \bar{u} taken at $x = 0.2$ m and $y = 0.1025$ m (longitudinal and lateral center of tank) from numerical results obtained in the grid sensitivity analysis. Spatial convergence is observed between the three finest meshes (1.48, 1.85 and 2.31 mm).

Table 2: Grid sensitivity analysis parameters

mesh	size (mm)	count [†]	$t^{\dagger\dagger}$ (h)	$\bar{\Phi}_{neg}$ (l/s)
1	1.48	3.1	80.24	0.690
2	1.85	1.6	33.33	0.746
3	2.31	0.97	11.8	0.726
4	2.89	0.45	4.3	0.469
5	3.61	0.25	3.7	0.495
6	4.51	0.13	3.3	0.43

Note: size indicates the lengths of each side of the hexahedra mesh elements of the interior of the domain, [†] total mesh size in millions of cells, $t^{\dagger\dagger}$ cpu clock-time to run 60 s of simulated flow on 192 AMD 2.2 GHz processors. Simulations performed using modeling parameters of f12SN (see section 2.11).

reduce the size of the computational domain. The resulting mesh consisted of 1 630 163 hexahedra cells. Though OpenFOAM solves strictly on an unstructured mesh topology, given the Cartesian nature of the hexahedra used with 0 non-orthogonality and 0 skewness, the mesh can be considered structured.

2.11. Numerical runs

Following a large number of preliminary numerical runs, only eight conditions developing the most valid flow fields were retained for further investigation. The base condition (b12SN, Table 3) was performed at a mass flow rate ($\dot{m}_a = 12$ g/min), a bubble diameter of $d_{mean} = 3.55$ mm, a C_{TD} value of 0.5, a C_{VM} value of 0.5 and the Schiller-Naumann model for drag force closure C_D . Lateral lift was introduced in run b12SNL and swarm correction was added in b12SNSw. In run b12IZ, the Ishii-Zuber drag closure model replaced the Schiller-Naumann model. The combined effects of lateral lift and swarm correction were intro-

Table 3: Details of simulation parameters

Simulation	\dot{m}_a (g/min)	C_{TD}	C_D	C_L	l	l
b12IZ	12	0.5	IZ	0.5	0.5	
b12SN	12	0.5	SN		0.5	
b12SNLf	12	0.5	SN	0.5	0.5	
b12SNSw	12	0.5	SN		0.5	1.75
f12SN	12	0.5	SN	0.5	0.5	1.75
f12IZ	12	0.5	IZ	0.5	0.5	1.75
f8IZ	8	0.5	IZ	0.5	0.5	1.75
f4IZ	4	0.5	IZ	0.5	0.5	1.75

Note: d_{mean} for all models was 12 g/min was 3.55 mm, except for simulations f8IZ and f4IZ whose d_{mean} values are presented in Table 3 for the corresponding value of \dot{m}_a . SN = Schiller-Naumann, IZ = Ishii-Zuber. Tomiyama swarm correction used with l . Simulations were performed on mesh 2 ($\Delta d = 1.85$ mm).

duced in run f12SN (f prefix indicates *full*). The effects of the Ishii-Zuber model on the full model were investigated in run f12IZ. Additional runs with identical parameters to f12IZ except at the two lower values of \dot{m}_a tested experimentally (4 and 8 g/min, f4IZ and f8IZ, respectively) were performed. Details of the numerical parameters used in each of the runs are presented in Table 3. Additional runs examining the effects of increasing the C_l coefficient from 0.5 to 1.25 on the f12IZ model (f12IZ $C_l=0.75$, f12IZ $C_l=1$, f12IZ $C_l=1.25$) is presented in section 3.8. The discretization schemes used are identical to those suggested in the standard *twoPhaseEulerFoam bubbleColumn* tutorial distributed with the OpenFOAM 5.0 release. The boundary conditions applied are also identical to those used in the *bubbleColumn* tutorial, except in 3D and, with an air inlet boundary patch placed on top of the diffuser using OpenFOAM’s *setSet* and *createPatch* utilities. Details of the boundary conditions and discretization schemes used are made available as supplementary material. Further details about the discretization schemes used and the boundary condition types applied can be found in the OpenFOAM user guide and in Moukalled et al. (2016).

3. Results and discussion

3.1. Experimental bubble diameter

Bubble diameters measured at $z' = 50$ mm and 150 mm for the three \dot{m}_a conditions tested are presented in Table 4. The mean bubble diameter increased by approximately 0.7 mm between the $\dot{m}_a = 4$ g/min and the $\dot{m}_a = 12$ g/min condition (t -test, $p < 1e-3$) at both levels of z' . However, only a minor (non-significant) increase in d_{mean} with increasing z' was observed (t -test, $p > 0.1$). The variation in d_{mean} with increased \dot{m}_a is likely owed to greater opportunity for bubble coalescence as $\bar{\alpha}_a$ increases with \dot{m}_a , and/or larger initial bubble diameters as they separate from the porous diffuser medium.

3.2. Volumetric flux and flow field at the yz_{x200} plane

Experimentally estimated $\bar{\Phi}_{neg}$ passing through the yz_{x200} plane in the $\dot{m}_a = 12$ g/min condition was estimated

to be 0.772 l/s from sPIV data (Table 5). Numerical predictions of $\bar{\Phi}_{neg}$ in each $\dot{m}_a = 12$ g/min run varied greatly from one another depending on the combination of interphase momentum transfer terms applied (Table 5). The Schiller-Naumann drag model coupled with lateral lift was most accurate at predicting the volumetric flux induced in the body of water by the rising bubble swarm. For example, the b12SNLf and f12SN models estimated $\bar{\Phi}_{neg}$ to be 0.666 and 0.746 l/s respectively.

The structure of the predicted flow fields was also affected by the choice of terms. The sPIV plane (Fig. 3a) showed high negative (towards the diffuser) \bar{u} values at $z < 50$ and strong positive \bar{u} values along the walls of the tank ($y > 60$ mm) for values of $z > 75$ mm. Maximum experimental values of positive \bar{u} of ≈ 0.14 m/s were measured in the upper right corner of the presented flow field at $z > 150$ and $y > 80$ mm. The numerical models also predicted maximum positive values of \bar{u} near the top corner and wall of the tank, yet values were $\approx 25\%$ lower than experimental values. Despite the f12SN run providing the closest $\bar{\Phi}_{neg}$ prediction, the 2D spatial distribution of \bar{u} differed substantially from that measured experimentally. The f12SN run predicted greater \bar{u} values at the tank’s mid-depth, and a stronger lateral \bar{u} gradient close to the bed compared to the sPIV data. Both the b12IZ and f12IZ runs (Fig. 3b, g) qualitatively provided better predictions of the spatial distribution of \bar{u} across the yz_{x200} plane than f12SN, yet underpredicted $\bar{\Phi}_{neg}$ by factors of 0.86 and 0.84, respectively. The results in Table 5 and Fig. 3 highlight the sensitivity of the two-phase modeling approach to the choice of interphase momentum transfer terms. For example, the Schiller-Naumann drag closure without lateral lift (i.e., b12SN and b12SNSw) drastically underpredicted $\bar{\Phi}_{neg}$ by factors of 0.54 and 0.57. Including the Tomiyama swarm correction with lateral lift (i.e., f12SN), improved the prediction of $\bar{\Phi}_{neg}$ compared to the same model without swarm correction (i.e., b12SNLf). The variability in $\bar{\Phi}_{neg}$ and the 2D spatial distribution of \bar{u} across the combinations of interphase momentum transfer terms studied stands in contrast to recommendations that only the drag force needs to be taken into account for predicting bubble induced recirculation (Balleda et al., 2007; Ali Basheer and Subramaniam, 2012).

3.3. 3D flow field

A portion of the 3D flow field for the 12 g/min condition was reconstructed from data interpolated from the multiplane sPIV experiment. The 3D sPIV flow field is presented in Fig. 4a juxtaposed with the predicted flow field of the f12IZ simulation (Fig. 4b). The f12IZ model is presented due to its fair accuracy at predicting $\bar{\Phi}_{neg}$ and reproducing the 2D \bar{u} velocity contours in Fig. 3a. The sPIV flow field can be broadly split into three regions: (1) a high velocity near-bed region extending from approximately $0 \text{ mm} < z < 50 \text{ mm}$ in which a substantial portion of the volumetric flux returns towards the diffuser; (2) a complex 3D recirculatory flow region demonstrating moderate velocity magnitudes in the central zone of the

Table 4: Bubble parameters measured from high-speed video.

z' (mm)	\dot{m}_a (g/min)	d_{mean} (mm)	$\pm \sigma_{d_{mean}}$ (mm)	\bar{w}_a (m/s)	$\pm \sigma_{\bar{w}_a}$ (m/s)
150	12	3.6	0.8	0.61	0.074
-	8	3.2	0.7	0.54	0.061
-	4	2.9	0.7	0.40	0.041
50	12	3.5	0.7	0.51	0.073
-	8	3.1	0.6	0.48	0.066
-	4	2.8	0.6	0.41	0.044

Note: z' indicates height above the diffuser inlet face.

Table 5: Experimental and numerical values of $\bar{\Phi}_{neg}$ at y_{xz200} .

Simulation	$\bar{\Phi}_{neg}$ (1/s)	$\bar{\Phi}_{neg}^i / \bar{\Phi}_{neg}^{sPIV}$
sPIV	0.772	-
b12IZ	0.587	0.76
b12SN	0.460	0.60
b12SNLf	0.666	0.86
b12SNSw	0.488	0.63
f12SN	0.746	0.97
f12IZ	0.649	0.84

tank ($50 \text{ mm} < z < 180 \text{ mm}$) and (3) a high velocity region near the side-wall consisting primarily of positive x directed flow (away from the diffuser). The f12IZ results differ from the sPIV results in important ways; the return velocity magnitudes (i.e., \bar{u}) are more evenly distributed over z ; the maximum near-bed values of \bar{u} are lower by $\approx 25\%$; the recirculatory central region is far less complex in structure; and the near side-wall positively x directed velocities are of lower magnitude ($\approx 25\%$ lower). Figure 5 shows the correspondence of numerical and sPIV values for \bar{u} over the entire y_{xz200} -plane (dotted blue line Fig. 4). The apparent difference in vector scale in the upper near-wall region of the flow in Figs. 4a and Figs. 4b is due primarily to the low predictions ($\approx 25\%$) of \bar{u} in the region of the flow delimited by the side-wall of the tank, $z > 150 \text{ mm}$ and $y > 70 \text{ mm}$ 5.

3.4. xz -centerplane flow field

In the analysis that follows, an emphasis is placed on the fiiIZ family of models due to the fair performance of the f12IZ model at predicting $\bar{\Phi}_{neg}$ and reproducing the 2D contours plots in Fig. 3. For the three values of \dot{m}_a studied, the numerical vector fields share many similarities to those measured experimentally with sPIV (Fig. 6), yet they also show a number of important differences. Generally, the main recirculatory pattern was well predicted over the three flow rates, with vector orientations aligning relatively well with those measured experimentally. The location of the stagnant core of the recirculatory flow was also well approximated (top right-hand corners, Fig. 6a, b, c) and the vector orientations of flow returning towards the diffuser also aligned well with experiments. Important deviations between the modeled and experimental flow fields for each \dot{m}_a condition are detailed in the proceeding subsections followed by a discussion of turbulence results for

all three \dot{m}_a conditions.

3.4.1. $\dot{m}_a = 4 \text{ g/min}$ condition

A preliminary qualitative observation of the $\dot{m}_a = 4 \text{ g/min}$ condition seeded with near-neutrally buoyant beads was performed to gain insights on the 3D structure of the flow field. This observation demonstrated the flow field near the diffuser ($x < 200 \text{ mm}$) to be composed principally of two recirculatory cells with their axes of rotation aligned parallel to the tank's longitudinal axis. A cell occupied either side of the $y = 0 \text{ mm}$ xz -centerplane, spanning from $35 \text{ mm} < x < 200 \text{ mm}$ and extending from the tank bottom to the near surface. Looking towards the diffuser, these cells rotate clockwise on the right hand side of the xz -centerplane and counter-clockwise on the left-hand side. The nearly vertical experimental vectors over the region between $x < 200 \text{ mm}$ and $z < 100 \text{ mm}$ and the tank walls (Fig. 6a) provides evidence of these recirculatory cells. The strong vertical components in this region occur where the two counter-rotating cells meet at the xz -centerplane as the flow ascends to the surface. Though the recirculatory cells were confirmed in the modeled f4IZ results (not shown), they were a less dominant feature of the near-diffuser flow field and varied considerably in morphology, as suggested by the discrepancy between the sPIV and f4IZ vectors between $x < 35 \text{ mm}$ and $x < 200 \text{ mm}$ in Fig. 6a.

For $x > 200 \text{ mm}$, experimental vectors become more horizontally aligned, indicating the flow in this region is no longer inside of the near-diffuser recirculatory cells. Higher in the tank ($y > 100$) in the near-diffuser region, f4IZ results match sPIV estimates well (Fig. 6a). Still high in the tank, yet farther from the diffuser ($x > 200 \text{ mm}$), vector magnitudes were underestimated in spite of the good predictions of orientation. The scatter plot of measured versus numerical \bar{w} in Fig. 7b clearly demonstrates the incorrect prediction of the velocity field in the far wall region. In Fig. 7b, the relatively strong negative \bar{w} (e.g., -0.025 to -0.05 m/s) values measured near the far wall were instead predicted to be $> -0.01 \text{ m/s}$. However, regions dominated by positive values of \bar{w} were better predicted, as witnessed by the general correlation of points in Fig. 7b in the positive-positive quadrant (top-right).

3.4.2. $\dot{m}_a = 8 \text{ g/min}$ condition

In the $\dot{m}_a = 8 \text{ g/min}$ condition, experimental vectors in the region enclosed between $x < 200 \text{ mm}$ and $z < 100$

mm and the tank's walls had less of a vertical component compared to the $\dot{m}_a = 4$ g/min (Fig. 6b). This suggests the counter-rotating cells have largely disappeared at this higher \dot{m}_a value, with the flow field instead developing a dominant recirculatory flow pattern extending the full length of the tank with an axis of rotation parallel to the tank's lateral axis. The f8IZ model accurately captured the main features of this flow pattern, as witnessed by the general agreement in vector orientation and magnitude in Fig. 6b. Of particular interest, is the f8IZ performance at predicting the near-bed velocity magnitudes $z < 25$ mm, which is apparent by the concentration of points near the line-of-unity in the negative-negative quadrant of the Fig. 7a. Nevertheless, vector magnitudes persisted to be underestimated along the far wall in the f8IZ results, as seen in the \bar{w} scatter being largely underpredicted in the negative-negative quadrant of Fig. 7b.

3.4.3. $\dot{m}_a = 12$ g/min condition

For the $\dot{m}_a = 12$ g/min f12IZ condition, vector directions and magnitudes qualitatively match experimental results across much of the xz -centerplane (Fig. 6)c. Vertical profiles of \bar{u} , \bar{w} and TKE taken at the x locations indicated as red lines in Fig. 6c ($x = 100, 200$ and 375 mm) are presented in Fig. 8 to compare correspondences between the modeled and experimental flow fields. All the tested models had difficulty predicting the experimental \bar{u} values at $x = 375$ mm (Fig. 8c). However, the f12IZ model largely outperformed the other models at predicting \bar{w} at $x = 375$ mm (Fig. 8f), yet still significantly underpredicted \bar{w} for $y < 100$ mm. Similar to $\dot{m}_a = 4$ and 8 g/min, in regions dominated by positive \bar{w} (the near-diffuser region, $x < 200$ mm) the numerical and experimental values of \bar{w} are highly correlated (positive-positive quadrant, Fig. 7b). This is also seen in Fig. 8d for f12IZ and the other two models including the lateral lift term (i.e., f12SN, b12SNLf).

Below $z \approx 50$ mm, flow was predicted to return towards the diffuser at a lower \bar{u} than measured experimentally. This is true not only of f12IZ, but also all the other models. The low values of \bar{u} near the tank floor are apparent in Fig. 7a, where points with the strongest negative values of sPIV \bar{u} (e.g., ≈ -0.15 m/s) were predicted to be ≈ -0.10 m/s in the f12SN results. The underprediction of \bar{u} is also evident in the xz -centerline vertical profiles in Figs. 8a, b.

Models containing the lateral lift term (i.e., f12IZ, f12SN and b12SNLf) provided the best predictions of $-\bar{u}_{max}$ in Fig. 8. Of note also, is that the f12IZ was the only model to underpredict the vertical location of the transition between $-\bar{u}$ and $+\bar{u}$ in Fig. 8a, b. This is the vertical position of the strong shear-zone occurring where the over-lying positively directed flow near the surface (moving away from the diffuser) transitions to flow returning towards the diffuser (see Fig. 3a). The f12SN model, in contrast, significantly over-predicts the location of this shear zone (Fig. 8a, b)

In section 3.2 it was shown that f12SN most closely predicted $\bar{\Phi}_{neg}$. This is despite f12SN developing vertical \bar{u} profiles distinct from measured profiles in Fig. 8b. The fairly accurate $\bar{\Phi}_{neg}$ prediction is largely owed to a vertical redistribution of \bar{u} . Underpredicted values of \bar{u} near

the bed are compensated by higher values of \bar{u} for $z > 50$ mm, where \bar{u}_{neg} begins to have a larger magnitude than measured values (Fig. 8a, b). Models without lateral lift, however, generally underpredict \bar{u} over the entire depth (Fig. 8a, b), therefore $\bar{\Phi}_{neg}$ values were also significantly underestimated (see section 3.2).

Despite the deviations in the far wall region and near the bed, the overall agreement in \bar{u} between sPIV and f12IZ is acceptable in Fig. 7a (least-squares regression slope of 0.62, $R^2 = 0.86$). The \bar{w} components over the central plane were underpredicted in the f12IZ model (least-squares regression slope of 1.14, $R^2 = 0.84$, Fig. 7b).

3.4.4. Turbulent kinetic energy

Experimentally measured turbulent kinetic energy (TKE) over the lateral center plane was generally < 0.005 m²/s². The dense cluster of points near the origin of Fig. 7c indicates the low levels of turbulence occurring across the majority of the plane. The low turbulence levels, even in the $\dot{m}_a = 12$ g/min condition are apparent in Fig. 8g, h, i, where for $z < 150$ mm, $TKE < \approx 0.003$ m²/s².

In the $\dot{m}_a = 12$ g/min condition, near the surface (i.e., $z > 150$ mm), TKE is in excess of 0.008 m²/s² over most of the longitudinal span of the tank (Fig. 8g, h) and decreases rapidly near the far wall (Fig. 8i). The high values of TKE closer to the bubble swarm are due to shear induced turbulence in the region between 150 mm $< z <$ 205 mm (see Fig. 3a). The majority of models underpredicted turbulence over this region, except for the f12IZ model, which closely matched the experimental vertical TKE profile at $x = 100$ mm (Fig. 8g) and over a significant portion of the profile in Fig. 8h. The good predictions of TKE in the f12IZ model is likely due to the better estimate of the \bar{u} vertical gradient over the 150 $< z <$ 205 region (Fig. 8a, b and Fig. 3a). The majority of runs predicted the transition from $-\bar{u}$ to $+\bar{u}$ to begin higher in the flow, explaining why the larger values of TKE for these models occur closer to the surface (Fig. 8a, b). In Fig. 7c, experimental and numerical vectors with the largest values of TKE were not collocated, likely due to the shift in the predicted location of the shear zone. This explains the large deviations observed in the scatter of Fig. 7c for values of $TKE > 0.005$.

3.5. Free-surface bulking

Maximum free-surface bulking at the lateral centerline along the wall nearest the diffuser (i.e., x and $y = 0$ mm) was measured to be $\Delta z_{max} = 6$ mm \pm 2 mm at $\dot{m}_a = 4$ g/min, 15 mm \pm 3 mm at $\dot{m}_a = 8$ g/min and 20 mm \pm 4 mm for $\dot{m}_a = 12$ g/min (Table 6). The numerical free-surface Δz_{max} results follow a similar increasing trend with increasing \dot{m}_a (i.e., f4IZ, f8IZ, and f12IZ, Table 6). Free-surface bulking was generally slightly overpredicted in the numerical results (Table 6).

Predicted longitudinal Δz profiles (i.e., $0 < x < 50$ mm) taken at $y = 0$ varied greatly across the $\dot{m}_a = 12$ g/min trials (not shown). For example, in the simulations without the lateral lift term (e.g., b12Sn, b12IZ) the free-surface

profiles were “humped”. In contrast, more gradually decreasing profiles of Δz were observed with lateral lift included. The variation in the free surface profiles across runs likely manifests from differences in the submerged bubble swarm morphology between runs. Despite these variations, the models acceptably predicted free-surface bulking and accurately captured the observed lowering of the free-surface with decreasing \dot{m}_a in the experimental results.

Table 6: Experimental and numerically predicted free-surface bulking.

Simulation	\dot{m}_a (g/min)	Δz_{max} (mm)	
		CFD	EXP.
b12IZ	12	21 ± 1.85	20 ± 4
b12SN	12	21 ± 1.85	20 ± 4
b12SNLf	12	21 ± 1.85	20 ± 4
b12SNSw	12	19 ± 1.85	20 ± 4
f12SN	12	19 ± 1.85	20 ± 4
f12IZ	12	19 ± 1.85	20 ± 4
f8IZ	8	17 ± 1.85	15 ± 3
f4IZ	4	13 ± 1.85	6 ± 2

Note: Δz_{max} is the maximum bulking of the free-surface above the initial water level of $z = 205$ mm in the tank.

3.6. Rise velocities

Bubble rise velocities (\bar{w}_a), measured with high-speed video, increased with height above the diffuser (z') and with increasing \dot{m}_a (Fig. 9 and Table 4). Predictions of \bar{w}_a for $\dot{m}_a = 12$ g/min increased with z' from ≈ 0.6 m/s at $z' = 50$ mm to values in excess of 0.8 m/s at $z' = 150$ mm. However, the maximum experimental value of \bar{w}_a was 0.77 m/s. In the \bar{w}_a profiles of Fig. 9a, the models not containing the lateral lift term (i.e., b12SN, b12SNSw, b12IZ) developed the highest values of \bar{w}_a (e.g., 0.9 to 1.1 m/s) and presented the steepest lateral gradients. In these models, the highest values of \bar{w}_a occurred at $y < 15$ mm and rapidly attenuate for $y > 15$ mm. This suggests these models developed a rapidly rising bubble swarm near the lateral center of the diffuser stone.

Including the lateral lift term produced profiles (i.e., b12SNLf, f12SN, f12IZ) with lower maximum values of \bar{w}_a , which declined following a more linear profile with increasing y compared to models without lateral lift, suggesting their bubble columns were more laterally diffused. In the $\dot{m}_a = 12$ g/min condition, the general over-prediction of \bar{w}_a in all models at $z' = 150$ mm and better predictions at $z' = 50$ mm, suggest the air phase was erroneously accelerated as it rose, resulting in underpredicted momentum transfer to the adjacent body of water. The very low predictions of $\bar{\Phi}_{neg}$ (see Table 5) in the models without lateral lift (i.e., b12SN, b12SNSw, b12IZ) is likely attributable to the strong overpredictions of \bar{w}_a in the air phase.

Similar to the $\dot{m}_a = 12$ g/min results, simulations f4IZ and f8IZ generally overpredicted measured values of \bar{w}_a at $y < 15$ mm. However, the profile averages of \bar{w}_a , for the f4IZ and f8IZ results presented in Fig. 9 were generally

within one standard deviation of \bar{w}_a measured experimentally (red-dotted lines Fig. 9b, c, e, f). Exceptionally, the f4IZ g/min at $z' = 50$ mm, which with a profile average of \bar{w}_a of 0.35 m/s, was below a standard deviation of the experimental mean of 0.41 m/s ± 0.044 m/s.

3.7. Void fraction

Measured void fractions ($\bar{\alpha}_a$) were highest nearest the diffuser surface for the three values of \dot{m}_a investigated (Fig. 10j,k,l). In the $\dot{m}_a = 12$ g/min condition, $\bar{\alpha}_a$ was in excess of 0.2 for much of the profile at 10 mm above the stone (Fig. 10j). At $z' = 50$ mm, the measured maximum values of $\bar{\alpha}_a$ are ≈ 0.10 for values of $y < 20$ mm and decrease further at higher values of z' . The lateral expansion of the bubble swarm as it rises is apparent for all three conditions of \dot{m}_a , as observed by the higher values of $\bar{\alpha}_a$ for $y > 30$ mm as z' increases.

Good agreement was observed between modeled and experimental values of $\bar{\alpha}_a$ at $z' = 10$ mm (Fig. 10). In the $\dot{m}_a = 12$ g/min condition at higher elevations, $\bar{\alpha}_a$ profiles varied greatly depending on the momentum transfer terms used in the runs, with some runs deviating substantially from measured profiles (Fig. 10a, d, g). Runs without the lateral lift term (i.e., b12SN, b12SNSw, b12IZ) tended to concentrate $\bar{\alpha}_a$ near the centerplane of the tank (i.e., $y < 15$ mm). In contrast, simulations including lateral lift (i.e., b12SNLf, f12SN, f12IZ) developed eccentric humps in their profiles persisting over the range of z' . The eccentricity of the predicted peak in $\bar{\alpha}_a$ values suggests the bubble swarm contained a column of concentrated $\bar{\alpha}_a$ rising between $|10| < y < |40|$ mm for these models. These columns were qualitatively observed to quasi-periodically appear during the trials at lower values of z' (e.g., < 50 mm). Evidence of their presence can be observed in the experimental data as the eccentric peaks of $\bar{\alpha}_a$ measured at $z' = 10$ mm (10j, k, l), however these peaks did not persist at higher values of z' profiles. It is speculated that the concentrated columns of air are due to incoming flow locally confining the bubbles during the early stage of their ascent.

The positions of the high values of $\bar{\alpha}_a$ at $y < 20$ mm in Fig. 10 for models without the lateral lift term (i.e. b12SN, b12SNSw, b12IZ), correspond with the positions of the highest values of \bar{w}_a for these models in the \bar{w}_a profiles presented in Fig. 9a. The high values of \bar{w}_a in Fig. 9a may have caused bubbles to be laterally entrained in their rising wake, resulting in the elevated values of $\bar{\alpha}_a$ observed for these models in Fig. 10a, d and g.

3.8. Lift coefficient

The preceding analysis demonstrated substantial improvements in predicted $\bar{\Phi}_{neg}$ and spatial distributions of \bar{u} over the yz_{x200} -plane in the models including the lateral lift term. In light of this, a sensitivity analysis of the f12IZ model to increases in the constant lift coefficient (C_l) was performed. The effects of three additional values of C_l (0.75, 1 and 1.25) on the following parameters were investigated: $\bar{\Phi}_{neg}$, the volume of the numerical bubble swarm V , the volume of air within the bubble swarm V_a

and the swarm-volume-average of \bar{w}_a . Table 7 resumes the parameters studied and the results of this analysis.

Considerable improvements were observed in the prediction of $\bar{\Phi}_{neg}$ with increasing C_l . With a C_l of 1.25, $\bar{\Phi}_{neg} = 0.798 \text{ l/s}$ compared to 0.772 l/s measured with sPIV (Table 7). Qualitatively, the 2D \bar{u} contours for f12IZ $_{Cl=1.25}$ (Fig. 11e) more closely predicted the experimentally measured values of \bar{u} near the bottom-center region of the tank (Fig. 3a) than the models with lower values of C_l or those presented in Fig. 3a-g. The maximum value of $-\bar{u}$ measured experimentally in this region was -0.137 m/s, those for f12IZ $_{Cl=0.5}$, f12IZ $_{Cl=0.75}$, f12IZ $_{Cl=1}$ and f12IZ $_{Cl=1.25}$ were -0.089 m/s, -0.094 m/s, -0.097 m/s and -0.106 m/s, respectively.

Despite the improved estimates of $\bar{\Phi}_{neg}$, the lower vertical extent of $+\bar{u}$ along the tank's wall (e.g., $y > 60 \text{ mm}$), erroneously lowers with increasing C_l . Experimentally, the lower extent of $+\bar{u}$ was $z \approx 75 \text{ mm}$ compared to $z \approx 50 \text{ mm}$ for the f12IZ $_{Cl=1.25}$ model. Similarly, the upper extent of $-\bar{u}$ moves higher with increasing C_l . In Table 7, the volume of the numerical bubble swarm (\bar{V}) increases with increasing C_l , while \bar{w}_a within this volume decreases. Despite the observed increase in bubble swarm volume, the values of V_a demonstrate that the volumes of air within each of the modeled bubble swarms remains constant. The findings of this analysis suggests that higher values of C_l tend to diffuse the bubble swarm laterally and longitudinally, causing it to occupy more volume, permitting a greater surface area to exchange momentum between the rising air and the water, thus resulting in lower \bar{w}_a and ultimately higher predictions of $\bar{\Phi}_{neg}$ circulating through the yz_{x200} -plane.

Table 7: Sensitivity of model f12IZ to variations in constant lift coefficient C_l

C_l	$\bar{\Phi}_{neg}$ (l/s)	\bar{V} (l)	\bar{w}_a (m/s)	V_a (l)
sPIV	0.772	-	-	-
0.5	0.698	0.199	0.469	0.031
0.75	0.693	0.220	0.449	0.031
1	0.735	0.234	0.439	0.030
1.25	0.798	0.262	0.419	0.031

Note: \bar{V} indicates the time-averaged volume of the bubble swarm, \bar{V}_a the time-averaged volume of air in the bubble swarm, \bar{w}_a time-average vertical velocity component of air in bubble swarm.

4. Conclusions

This study has investigated the ability of an unsteady Reynolds-averaged Euler-Euler approach to model the flow field of a bubble induced recirculatory flow in a laboratory tank. Stereoscopic particle image velocimetry (sPIV) permitted the experimental measurement of the time-averaged 3-component (\bar{u} , \bar{v} , \bar{w}) 3-dimensional (3C-3D) and 3C-2D turbulent flow field of the tank. The recirculatory flow induced by the rising bubbles is expected to be of similar 3D complexity to that expected in a full scale

waste-water grit-chamber. Air was injected through a diffuser fixed to the bottom of the tank at three mass flow rates (4, 8 and 12 g/min). Numerical runs of the tank using OpenFOAM's *twoPhaseEulerFoam* solver were performed with a variety of inter-phase momentum transfer closure combinations and a mixture $k-\epsilon$ turbulence viscosity closure. Numerical predictions were also compared to: experimental void fraction distributions (i.e., air concentrations) obtained using an fiber optic void fraction probe; average bubble rise velocities; and free-surface bulking measurements using high-speed videography techniques.

Models not considering lateral lift did not perform well. In particular they: underestimated $\bar{\Phi}_{neg}$ by upwards of 40%; overpredicted \bar{w}_a ; strongly underpredicted near-bed values of \bar{u} and developed unrealistic void fraction concentrations along the vertical centerline axis of the diffuser stone. Including the lateral lift term improved predictions of all the aforementioned metrics. An analysis of the constant lateral lift coefficient C_l revealed the model's considerably sensitivity to C_l . Indeed, a C_l coefficient of upwards of 1.25 was necessary to accurately predict $\bar{\Phi}_{neg}$ with the Ishii-Zuber drag closure model. This value of C_l is beyond the generally used range of 0.01 to 0.5 (Auton, 1987; Behzadi et al., 2004; Yeoh and Tu, 2006; Marschall et al., 2011a; Colombo and Fairweather, 2019). The volume of the bubble swarm was found to increase with increasing C_l , suggesting higher values of C_l act to laterally and longitudinally diffuse the bubble swarm. The increases in bubble swarm volume were accompanied by reductions in volume averaged \bar{w}_a , indicating greater momentum transfer between the rising bubbles and the fluid phase. This phenomena explains the increasing accuracy of the $\bar{\Phi}_{neg}$ predictions with greater values of C_l . Despite the improved predictions of the volumetric flux with lateral lift included, the predicted 3D flow field was considerably less complex in character compared to that measured experimentally with multiplane-sPIV. Vertical velocity and turbulence profiles also deviated from experimental values in many respects. Of particular interest were the models' underpredictions of near-bed \bar{u} values of $\approx 25\%$ and the inability of the models to predict the flow field direction and magnitude near the far wall of the tank.

This work was performed to evaluate the Euler-Euler approach for modeling a 3D flow field of greater complexity to those previously reported in the literature prior to investigating multiphase Eulerian modeling approaches to study sediment transport phenomena. However, the limitations of the model for predicting many important features of the 3D flow field suggests additional work is necessary to identify more appropriate interphase momentum transfer and turbulence closures. Additional improvements in flow field predictions may be gained by resolving the largest, most energetic scales of turbulence with either large-eddy or detached-eddy simulations. Future work aimed towards developing a more generalized lateral lift closure for highly 3D two-phase flows should help generalize the Euler-Euler approach for use in a wider range of industrial applications. However, limitations aside, many of the dominant features of the flow field were reproduced with acceptable

accuracy, demonstrating the potential of a properly calibrated Euler-Euler unsteady RANS approach for virtual prototyping grit-chamber designs.

5. Acknowledgements

The authors would like to thank the Natural Science and Engineering Council of Canada for providing the funding necessary to pursue this research. The authors also extend their gratitude to LaSalle|NHC (Northwest Hydraulic Consultants Inc.) for lending the optical probe used in this study. We also thank Nicolas Simard for his technical assistance with setting up the experimental apparatus. The simulations were performed using Mammouth Parallel-2B financed by the Canadian Foundation for Innovation, the Ministère de l'Économie, de la Science et de l'Innovation du Québec (MESI) and the Fonds de Recherche du Québec - Nature et Technologies (FQRNT). Many thanks go to all these organizations for supporting the infrastructure necessary to perform research requiring highly parallelized computing.

Nomenclature:

Acronyms

CFD	computational fluid dynamics
FOV	field of view
GUI	graphical user interface
HSV	high-speed video
IZ	Ishii-Zuber
PIV	particle image velocimetry
PIV	planar particle image velocimetry
S.D.	standard deviation
SN	Schiller-Naumann
sPIV	stereoscopic particle image velocimetry
VOF	volume-of-fluid
VTK	Visualization toolkit

Dimensionless numbers

C_D	drag coefficient [-]
C_D^e	ellipsoidal drag coefficient [-]
C_D^s	swarm corrected drag coefficient [-]
C_L	lateral lift coefficient [-]
C_{TD}	turbulent dispersion coefficient [-]
C_{VM}	virtual mass coefficient [-]
E_o	Eötvös number [-]
l	swarm correction coefficient [-]
R_{em}	mixture Reynolds number [-]
R_e	bubble Reynolds number [-]

Greek Symbols

α	phase fraction [-]
----------	--------------------

ϵ turbulence dissipation rate [$L^{-2}t^{-2}$]

μ dynamic viscosity [$ML^{-1}T^{-1}$]

ν kinematic viscosity [M^2T^{-1}]

ω vorticity [T^{-1}]

ρ phase density [ML^{-3}]

σ standard deviation

σ surface tension coefficient [MT^{-2}]

Subscripts, superscripts, overlines

$\bar{\phi}$ time-averaged value of ϕ

ϕ' fluctuating value of ϕ

ϕ^e ellipsoidal value of ϕ

ϕ^s spherical value of ϕ

ϕ_φ phase value of ϕ

ϕ_a gaseous phase (air) value of ϕ

ϕ_m mixture value of ϕ

ϕ_w liquid phase (water) value of ϕ

Symbols

F forces [MLT^{-2}]

F_D drag force [MLT^{-2}]

F_L lateral lift force [MLT^{-2}]

F_{TD} turbulent dispersion force [MLT^{-2}]

F_{VM} virtual mass force [MLT^{-2}]

g gravitational acceleration [LT^{-2}]

R^{eff} effective Reynolds stress [$MT^{-2}L$]

U phase velocity [LT^{-1}]

U_r relative (slip) velocity [LT^{-1}]

$^{\circ}C$ degrees Celsius

\dot{m} mass flow rate [MT^{-1}]

\overline{V}_a volume of air within numerical bubble swarm [L^3]

\overline{V} volume of numerical bubble swarm [L^3]

d_a mean bubble diameter [L]

h_{FOV} height field of view [L]

k turbulent kinetic energy [Θ]

M molar mass of dry air [MN^{-1}]

N_{FOV} frames in field of view [-]

p pressure [$MT^{-2}L$]

Q_{air} volumetric flow rate of air [L^3T^{-1}]

R gas constant of dry air [$ML^2T^{-2}\Theta^{-1}N^{-1}$]

R^2 coefficient of determination

T in degrees Kelvin [Θ]

t time [T]

TKE turbulent kinetic energy [Θ]

u velocity component along the x -axis [LT^{-1}]

v velocity component along the y -axis [LT^{-1}]

v_a	superficial velocity of air exiting diffuser surface [LT^{-1}]
w	velocity component along the w -axis [LT^{-1}]
x	longitudinal axis [L]
y	lateral axis [L]
z	vertical axis [L]
z'	distance above diffuser inlet surface [L]

6. References

- Ali Basheer, A., Subramaniam, P., 2012. Hydrodynamics, mixing and selectivity in a partitioned bubble column. *Chemical Engineering Journal* 187, 261–274. doi:10.1016/j.cej.2012.01.078.
- Auton, T.R., 1987. The lift force on a spherical body in a rotational flow. *Journal of Fluid Mechanics* 183, 199–218. doi:10.1017/S002211208700260X.
- Balleda, A., Pushpavananam, S., Deshpande, A., 2007. Experimental and numerical investigation of liquid circulation induced by a bubble plume in a baffled tank. *Chemical Engineering Science* 62, 4689–4704. doi:10.1016/j.ces.2007.05.023.
- Behzadi, A., Issa, R.I., Rusche, H., 2004. Modelling of dispersed bubble and droplet tow at high phase fractions. *Chemical Engineering Science* 59, 759–770. doi:10.1016/j.ces.2003.11.018.
- Bhusare, V.H., Dhiman, M.K., Kalaga, D.V., Roy, S., Joshi, J.B., 2017. CFD simulations of a bubble column with and without internals by using OpenFOAM. *Chemical Engineering Journal* 317, 157–174. doi:10.1016/j.cej.2017.01.128.
- Bhusare, V.H., Kalaga, D.V., Dhiman, M.K., Joshi, J.B., Roy, S., 2018. Mixing in a co-current upflow bubble column reactors with and without internals. *Canadian Journal of Chemical Engineering* 96, 1957–1971. doi:10.1002/cjce.23162.
- Brenner, A., Diskin, M.H., 1992. Model Study of Jet-circulated Grit Chamber. *Journal of Environmental Engineering* 117, 782–787.
- Colombo, M., Fairweather, M., 2019. Influence of multiphase turbulence modelling on interfacial momentum transfer in two-fluid eulerian-eulerian cfd models of bubbly flows. *Chemical Engineering Science* 195, 968–984. doi:10.1016/j.ces.2018.10.043.
- Dapelo, D., Alberini, F., Bridgeman, J., 2015. Euler-Lagrange CFD modelling of unconfined gas mixing in anaerobic digestion. *Water Research* 85, 497–511. doi:10.1016/j.watres.2015.08.042.
- Dutta, S., Tokyay, T.E., Cataño-Lopera, Y.A., Serafino, S., Garcia, M.H., 2014. Application of computational fluid dynamic modelling to improve flow and grit transport in Terrence J. O'Brien Water Reclamation Plant, Chicago, Illinois. *Journal of Hydraulic Research* 52, 759–774. doi:10.1080/00221686.2014.949883.
- Enrique Juliá, J., Harteveld, W.K., Mudde, R.F., Van den Akker, H.E.A., 2005. On the accuracy of the void fraction measurements using optical probes in bubbly flows. *Review of Scientific Instruments* 76, 035103. doi:10.1063/1.1862192.
- Gosavi, S., Kulkarni, N., Mathpati, C.S., Mandal, D., 2018. CFD modeling to determine the minimum fluidization velocity of particles in gas-solid fluidized bed at different temperatures. *Powder Technology* 327, 109–119. doi:10.1016/j.powtec.2017.12.026.
- Greenshields, C.J., 2017. OpenFOAM user guide version 5. July, OpenFOAM Foundation Ltd.
- Ishii, M., Zuber, N., 1979. Drag coefficient and relative velocity in bubbly, droplet or particulate flows. *American Institute of Chemical Engineers Journal* 25, 843–855.
- Kerdouss, F., Bannari, A., Proulx, P., 2006. CFD modeling of gas dispersion and bubble size in a double turbine stirred tank. *Chemical Engineering Science* 61, 3313–3322. doi:10.1016/j.ces.2005.11.061.
- Khan, Z., Bhusare, V.H., Joshi, J.B., 2017. Comparison of turbulence models for bubble column reactors. *Chemical Engineering Science* 164, 34–52. doi:10.1016/j.ces.2017.01.023.
- Lahey, R.T., 2005. The simulation of multidimensional multiphase flows. *Nuclear Engineering and Design* 235, 1043–1060. doi:10.1016/j.nucengdes.2005.02.020.
- Liu, Y.F., Hinrichsen, O., 2013. Numerical Simulation of Tube Erosion in a Bubbling Fluidized Bed with a Dense Tube Bundle. *Chemical Engineering and Technology* 36, 635–644. doi:10.1002/ceat.201200625.
- Lubchenko, N., Magolan, B., Sugrue, R., Baglietto, E., 2018. A more fundamental wall lubrication force from turbulent dispersion regularization for multiphase cfd applications. *International Journal of Multiphase Flow* 98, 36–44. doi:10.1016/j.ijmultiphaseflow.2017.09.003.
- Marschall, H., Mornhinweg, R., Kossmann, A., Oberhauser, S., Langbein, K., Hinrichsen, O., 2011a. Numerical Simulation of Dispersed Gas/Liquid Flows in Bubble Columns at High Phase Fractions using OpenFOAM®. Part I - Modeling Basics. *Chemical Engineering & Technology* 34, 1311–1320. doi:10.1002/ceat.201100161.
- Marschall, H., Mornhinweg, R., Kossmann, A., Oberhauser, S., Langbein, K., Hinrichsen, O., 2011b. Numerical Simulation of Dispersed Gas/Liquid Flows in Bubble Columns at High Phase Fractions using OpenFOAM®. Part II - Numerical Simulations and Results. *Chemical Engineering & Technology* 34, 1321–1327. doi:10.1002/ceat.201100162.
- Moukalled, F., Mangani, L., Darwish, M., 2016. The Finite Volume Method in Computational Fluid Dynamics. volume 113. Springer International Publishing. doi:10.1007/978-3-319-16874-6.
- Panda, S.K., Singh, K.K., Shenoy, K.T., Buwa, V.V., 2017. Numerical simulations of liquid-liquid flow in a continuous gravity settler using OpenFOAM and experimental verification. *Chemical Engineering Journal* 310, 120–133. doi:10.1016/j.cej.2016.10.102.
- Rusche, H., 2002. Computational Fluid Dynamics of Dispersed Two-Phase Flows at High Phase Fractions. PhD Thesis 1, 335. doi:10.1145/1806799.1806850.
- Shi, P., Rzehak, R., 2018. Bubbly flow in stirred tanks: Euler-Euler/RANS modeling. *Chemical Engineering Science* 190, 419–435. doi:10.1016/j.ces.2018.06.001.
- Tomiyama, A., Kataoka, I., Fukuda, T., Sakaguchi, T., 1995. Drag coefficients of bubbles: 2nd report, drag coefficient for a swarm of bubbles and its applicability to transient flow. *Transactions of the Japan Society of Mechanical Engineers Series B* 61, 2810–2817. doi:10.1299/kikaib.61.2810.
- Tomiyama, A., Tamai, H., Zun, I., Hosokawa, S., 2002. Transverse migration of single bubbles in simple shear flows. *Chemical Engineering Science* 57, 1849–1858.
- Wei, P., Mudde, R.F., Uijttewaal, W., Spanjers, H., van Lier, J.B., de Kreuk, M., 2019. Characterising the two-phase flow and mixing performance in a gas-mixed anaerobic digester: Importance for scaled-up applications. *Water Research* 149, 86–97. doi:10.1016/j.watres.2018.10.077.
- Yeoh, G., Tu, J., 2006. Two-fluid and population balance models for subcooled boiling flow. *Applied Mathematical Modelling* 30, 1370–1391. doi:10.1016/j.apm.2006.03.010.
- Zhongchun, L., Xiaoming, S., Shengyao, J., Jiyang, Y., 2014. Numerical investigation on lateral migration and lift force of single bubble in simple shear flow in low viscosity fluid using volume of fluid method. *Nuclear Engineering and Design* 274, 154–163. doi:10.1016/j.nucengdes.2014.04.011.

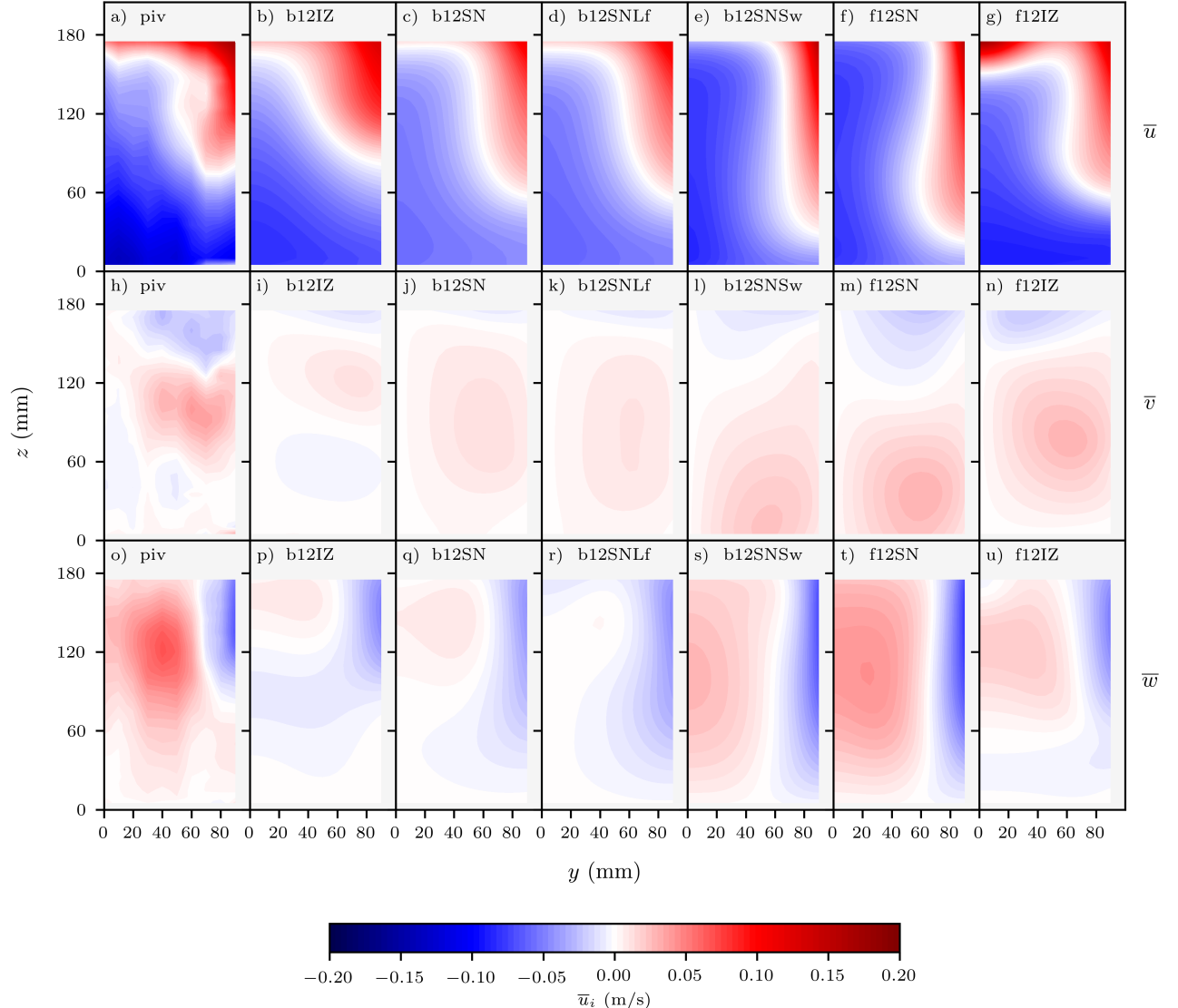


Figure 3: Cross-sectional yz -planes of \bar{u} (top-row), \bar{v} (middle-row) and \bar{w} (bottom-row) taken at $x = 200$ mm. The yz_{x200} plane was used as the surface of integration for $\bar{\Phi}_{neg}$ (Eq. 22). Blue indicates flow returning towards the diffuser (i.e., out of the page). Gray areas delineate non-measurable regions of the flow with sPIV due to strong laser reflections off bubbles near the free surface. High positive \bar{u} (red) is expected at $z > 175$ mm in the experimental data. Flow field is axisymmetric across the centerline $y = 0$ mm axis.

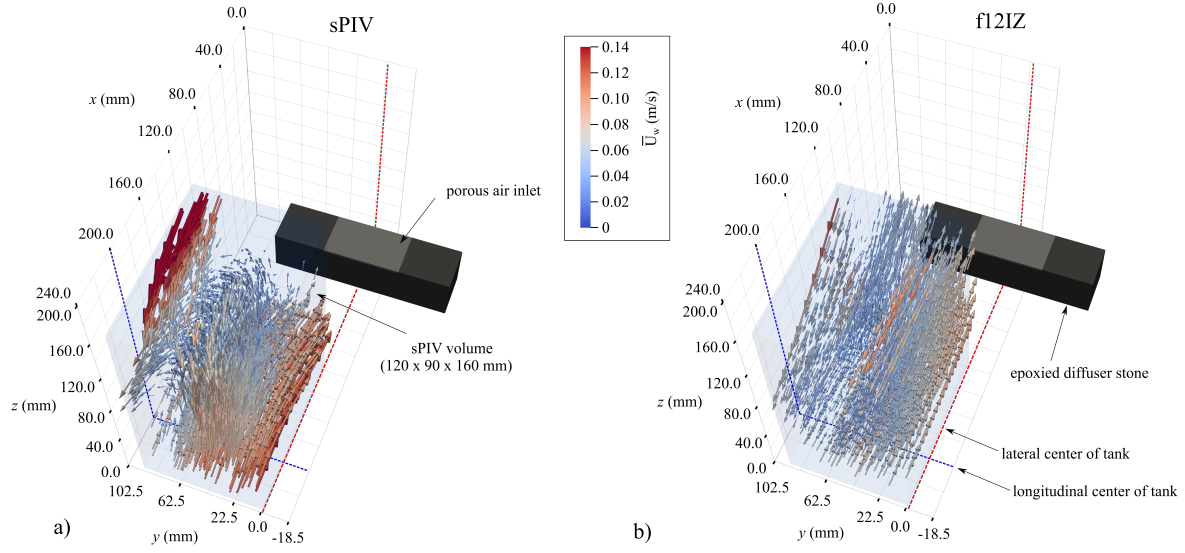


Figure 4: Experimental (a, sPIV) and predicted (b, f12IZ) time-averaged vector fields over a volume of the tank delineated by the limits $120 \text{ mm} < x < 240 \text{ mm}$, $0 \text{ mm} < y < 90 \text{ mm}$, $10 \text{ mm} < z < 175 \text{ mm}$. Flow fields are axisymmetric across the lateral center-plane of the tank. Blue transparent overlays outline the extents of the volume, which if mirrored over the lateral centerline, would represent 22% of the available tank volume. Experimental vector field (sPIV, $\dot{m}_a = 12 \text{ g/min}$) obtained by interpolating multiplane sPIV to a Cartesian grid ($5 \text{ mm} \times 5 \text{ mm} \times 5 \text{ mm}$). Vector magnitudes calculated as $\bar{U}_w = \sqrt{\bar{u}^2 + \bar{v}^2 + \bar{w}^2}$. Vectors scaled to \bar{U}_w (e.g., water). The f12IZ condition is depicted in (b) because it best estimated $\bar{\Phi}_{neg}$ in Table 5.

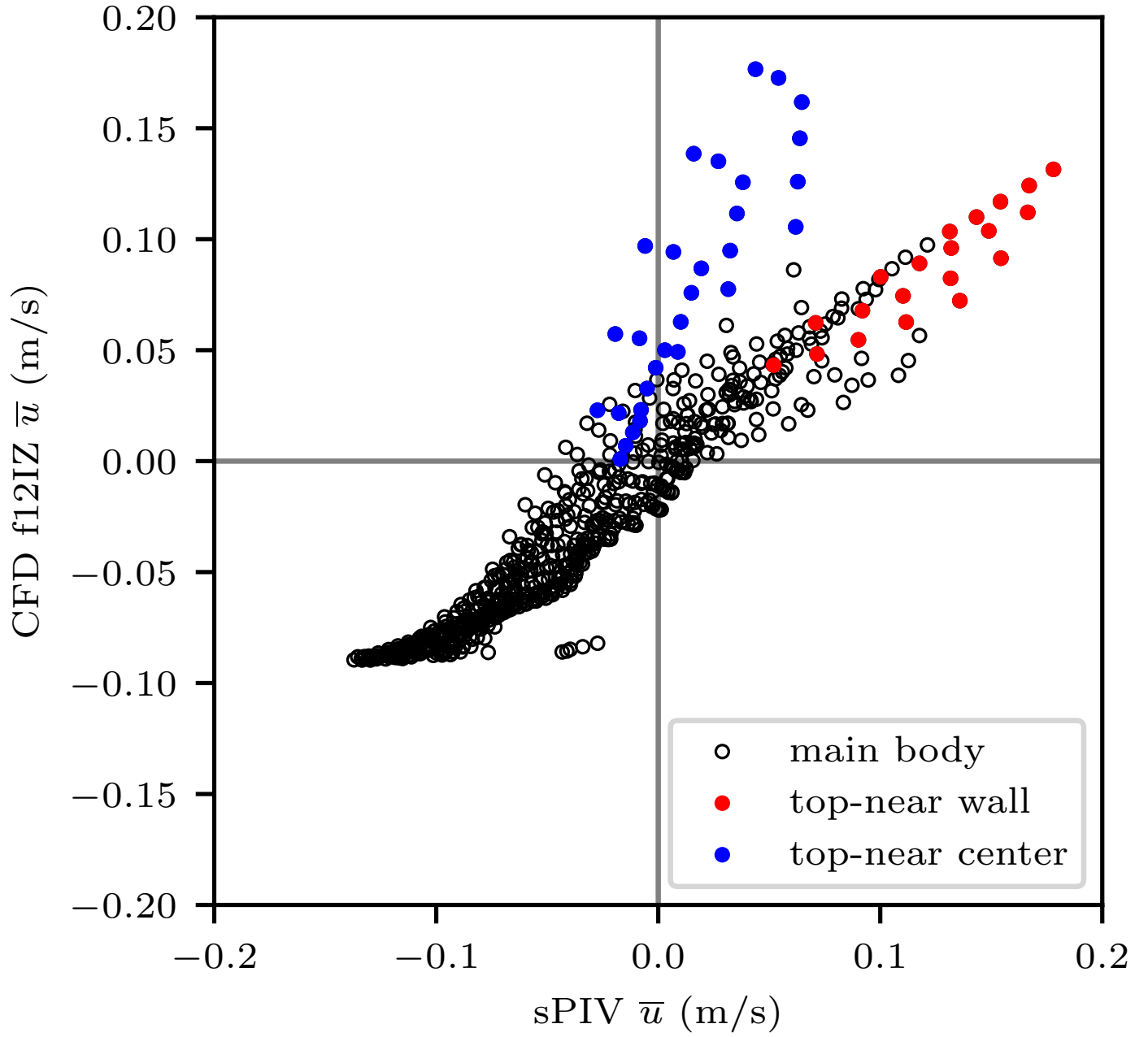


Figure 5: Comparative scatter plot of experimental and numerical \bar{u} taken over the yz_{x200} -plane (position indicated by dotted blue line in Fig. 4). Red points indicate values between the tank's walls and $z > 150$ mm and $y > 70$ mm. Blue points indicate values for $z > 150$ mm and $y < 30$ mm. Black points are for samples taken elsewhere on the plane.

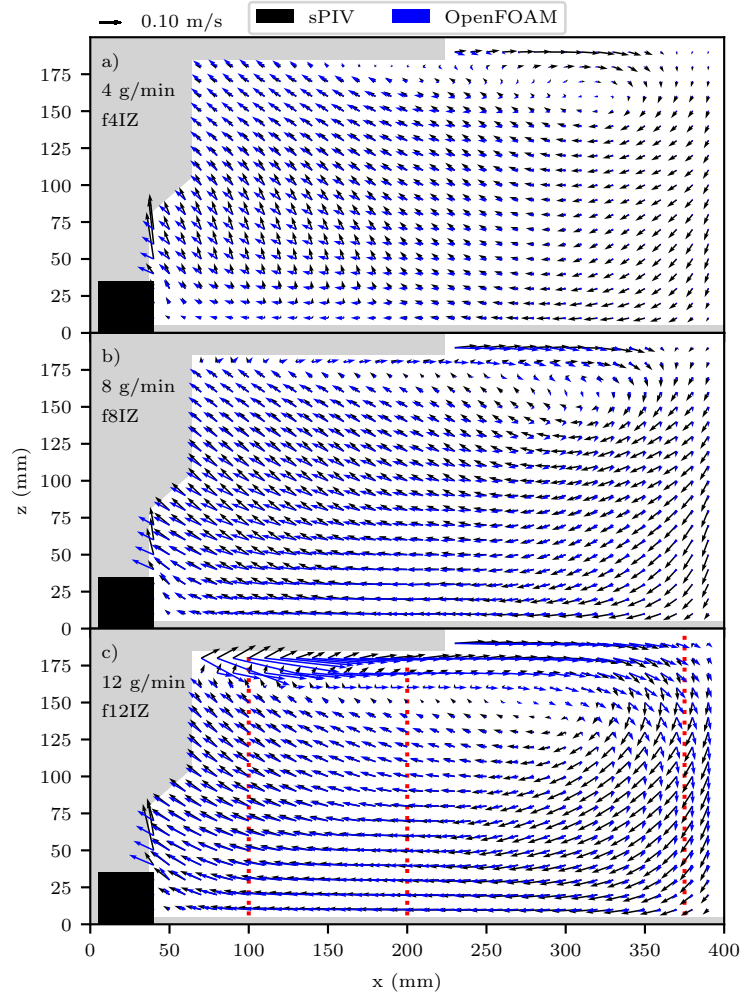


Figure 6: Comparative vector plots of experimental (sPIV) (black) and numerical (blue) of (a) f4IZ, (b) f8IZ and (c) f12IZ time-averaged 2D flow fields over the $y = 0$ mm xz -centerplane of the tank. Vector magnitudes calculated as $\overline{U_w} = \sqrt{\overline{u^2} + \overline{w^2}}$ (liquid phase). Experimental vector fields were reconstructed from the two sPIV planes (Fig. 1b) used to measure the velocity field along the $y = 0$ xz -centerplane of the tank. Grayed-out regions were inaccessible to sPIV measurement due to laser reflections off of bubbles. Red dotted lines in (c) indicate positions of vertical profiles presented in Fig. 8.

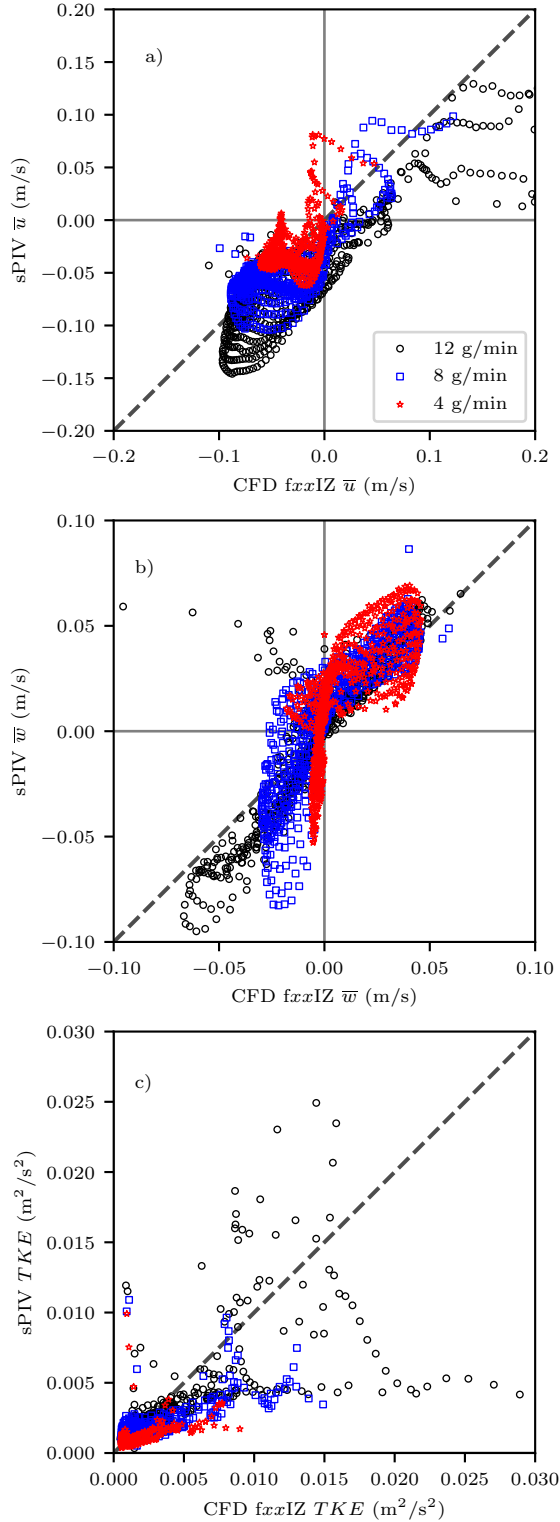


Figure 7: Comparison of experimental and numerical (fxxIZ family of models) \bar{u} (a) and \bar{w} (b) components of the vectors presented in Fig. 6. The turbulent kinetic energy (TKE) for each vector position in Fig. 6 are presented in c). Turbulent kinetic energy was calculated as $TKE = 0.5(\bar{u}^2 + \bar{v}^2 + \bar{w}^2)$. Dashed gray lines indicate lines of perfect correspondence between modeled and experimental results (line-of-unity).

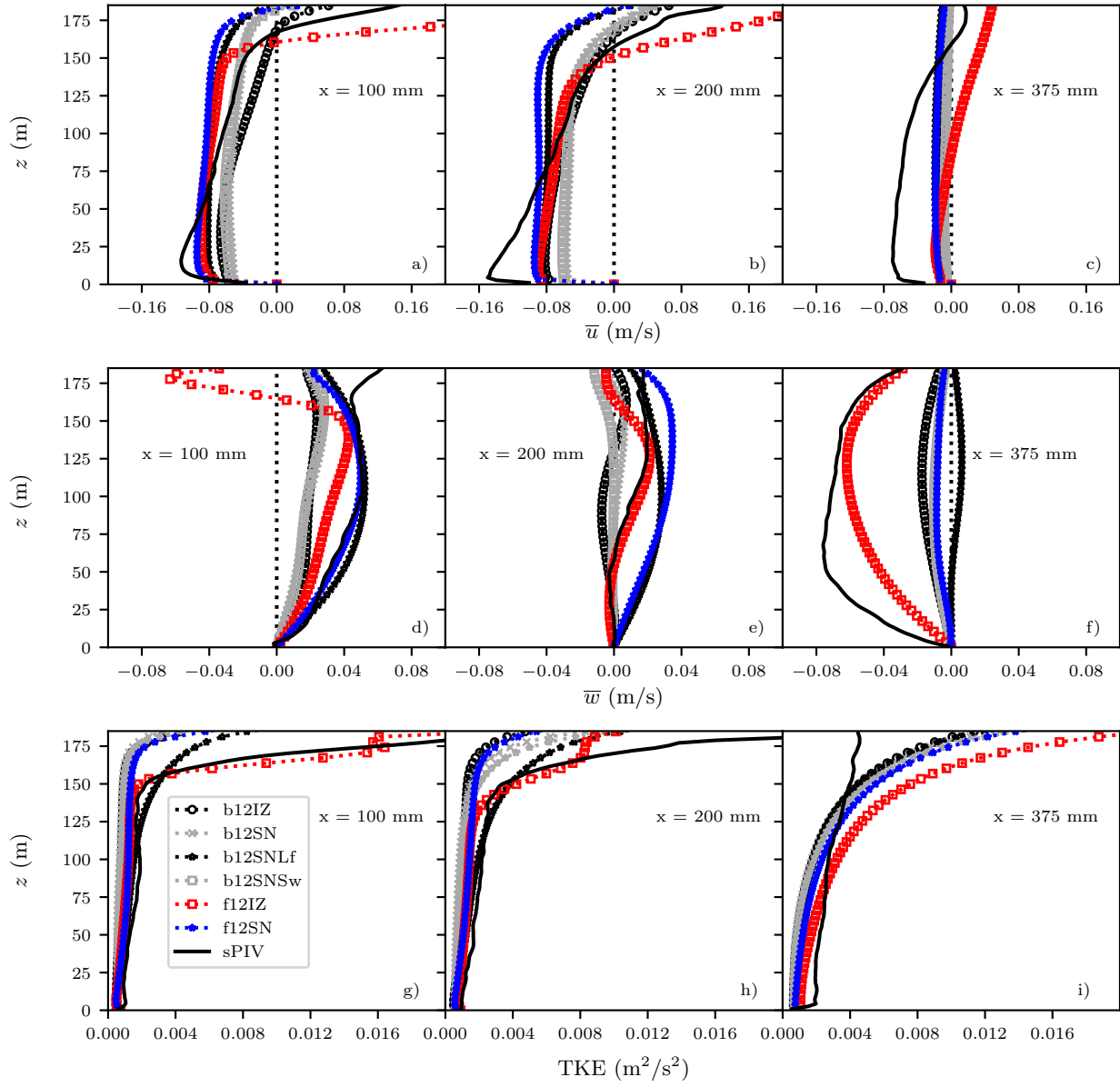


Figure 8: Centerline ($y = 0$ mm) vertical profiles of experimental (sPIV) and numerical results of \bar{u} (a, b, c), \bar{w} (d, e, f) and TKE (g, h, i) for $\dot{m}_a = 12$ g/min. The longitudinal locations of the profiles along the xz -centerplane are shown as dotted red lines in Fig. 6c.

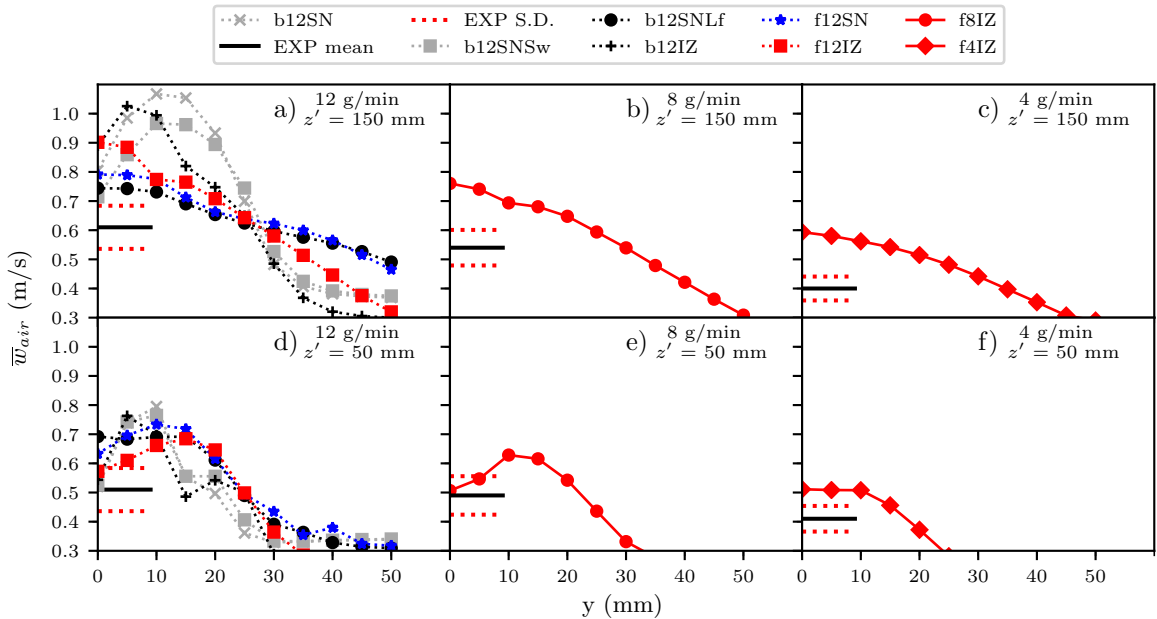


Figure 9: Numerical and experimental temporally averaged bubble swarm rise velocities (\bar{w}_a). Top row (a-c) presents findings for $z' = 150$ mm. Bottom row (d-f) presents findings for $z' = 50$ mm. Solid black lines indicate experimental average \bar{w}_a and dotted red lines indicate one standard deviation about the mean (i.e., $\sigma_{\bar{w}_a}$). Black lines span the lateral field of view of the high-speed video used to experimentally estimate \bar{w}_a .

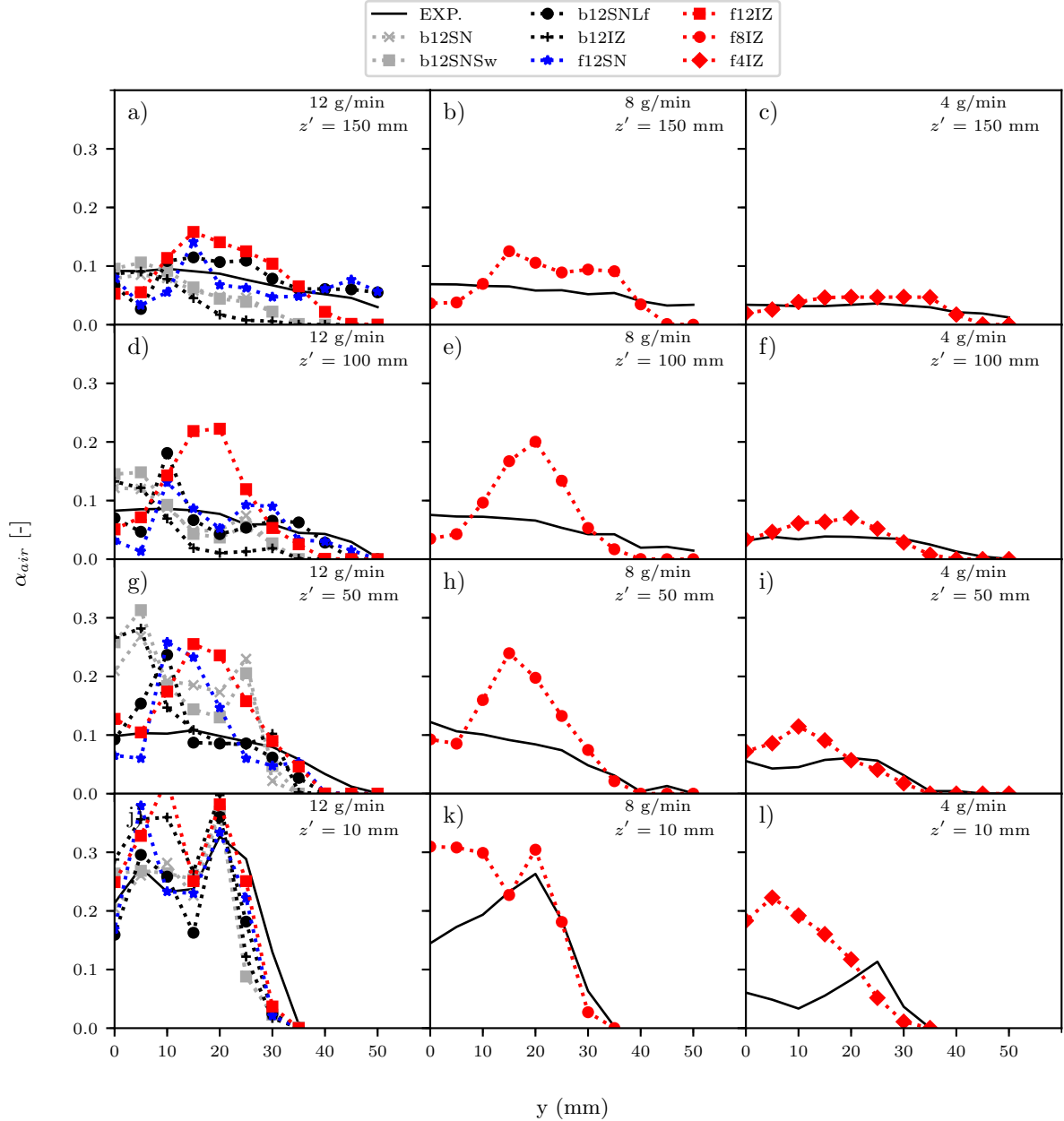


Figure 10: Experimental and numerical void fraction ($\bar{\alpha}_a$) measurements taken at four values of z' above the diffuser stone inlet ($z' = 10 \text{ mm}$, 50 mm , 100 mm and 150 mm). The diffuser inlet is positioned at $z = 35 \text{ mm}$ above the bed (i.e., $z' = 0 \text{ mm}$). The lateral center of the diffuser stone is at $y = 0$. Only half the lateral profile of the bubble swarm profile is shown because of symmetry across the $y = 0 \text{ mm}$ xz plane. Profiles were taken at the longitudinal center of the stone (i.e., $x = 22.5 \text{ mm}$).

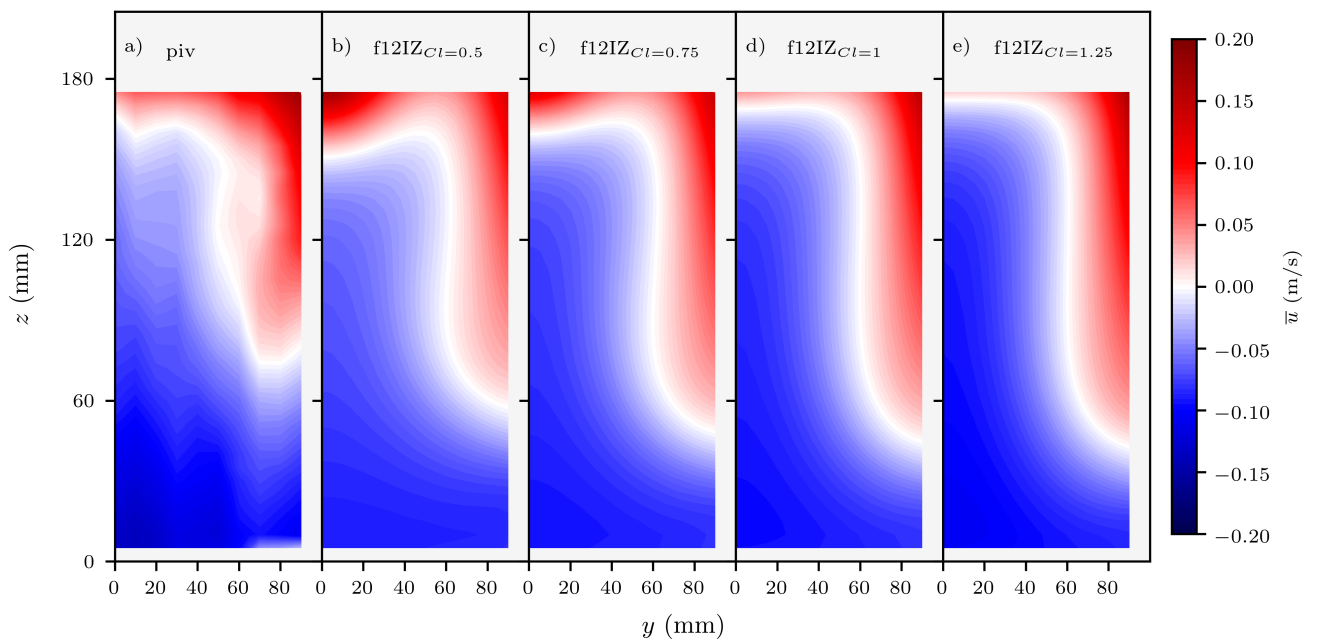


Figure 11: Variation of the 2D spatial distribution of \bar{u} over the yz_{x200} plane with increasing values of the lateral lift coefficient C_l .